國立臺灣大學 電機資訊學院 光電工程學研究所

碩士論文

Graduate Institute of Photonics and Optoelectronics

College of Electrical Engineering and Computer Science

National Taiwan University

Master’s Thesis

長共振腔之銦鎵鋁砷/磷化銦 脊型波導分佈反饋雷射的光電與熱效應研究

A photonic and thermal study on InAlGaAs/InP based long-resonant-cavity ridge waveguide distributed feedback lasers

鄭仲辰

Cheng, Chung-Chen

指導教授：林建中 博士

Advisor: Lin, Chien-Chung Ph.D.

中華民國一百一十三年十二月

December 2024

doi:10.6342/NTU202404706

摘要

利用向聯亞光電工業股份有限公司所購買的事先已有製作週期性光柵的 InP 磊晶片來製作出在長度與寬度上不同組合搭配的分布式回饋雷射（Distributed Feedback, DFB）元件。實驗內容囊括一開始的光罩、製程設計、元件製程進行與問題解決，再到最後對各尺寸元件的電性和發光特性(光功率、光譜分布)進行量測。

光罩上將元件設計為共振腔尺寸長 300/500/750/1250 μm，同時搭配寬度 2/4/6 μm，一共 12 種不同元件尺寸。

製程上在製作脊型波導共振腔時，由於元件的最小寬度在 2 μm，波導兩側的向下蝕刻採用乾蝕刻而非濕蝕刻，避免脊型波導的形狀因側向蝕刻或披覆層的包覆性不佳而被破壞。另外在透過電漿輔助化學氣相沈積(PECVD)沉積鈍化層氮化矽Si_3N_4後，同樣受限於元件尺寸，在定義掩膜開洞時採用自我對準[1]的技術，避免可能遭遇的曝光機的繞射極限以及人為對準失誤。

最後就成品的元件表現(功率、頻譜模態、熱......等)去探討在過程中可能出現的失誤。

關鍵詞: 長共振腔、脊型波導、分布式回饋雷射、自我對準、InAlGaAs、InP

doi:10.6342/NTU202404706

Abstract

This study utilizes InP epitaxial wafer, which is previously procured from *LandMark Optoelectronics Corporation*, to fabricate Distributed Feedback (DFB) laser devices with various combinations of lengths and widths. The experimental process includes the design of photomasks, process planning, device fabrication with troubleshooting, and the analysis of the electrical and optical characteristics (optical power and spectral distribution) of the devices.

The DFB laser devices were designed with resonant cavity lengths of 300, 500, 750, 1250 μm, paired with widths of 2,4, and 6 μm, resulting in a total of 12 device sizes respectively.

Due to the minimum width of the devices was set at 2 μm, a dry etching process was implemented for the shape of waveguide instead of wet etching to preserve the shape of the ridge waveguide and avoid damage from lateral etching or poor conformality of the deposited film layer.

Furthermore, after depositing a passivation layer of silicon nitride (Si_3N_4) via Plasma-Enhanced Chemical Vapor Deposition (PECVD), self-aligned[1] techniques were adopted for the mask opening. This approach mitigated potential issues related to the diffraction limit of the mask aligner and manual alignment errors by human since the minimum width of the devices mentioned above.

Index Terms: Long Cavity Length, Ridge Waveguide, Distributed Feedback Laser, Self-Aligned, Indium Aluminum Gallium Arsenide (InAlGaAs), Indium Phosphide (InP)

doi:10.6342/NTU202404706

致謝

就讀國立台灣大學光電工程研究所的二餘年間，萬分地感謝遇到的所有人、事、物。首要先感謝的是我的指導教授 林建中教授，作為一個好的師長，總是讓我們在研究上、課業上一遇到問題時便能馬上解惑，並且從中學習。老師也不忘在研究之餘關心著實驗室成員們的生活大小事、提醒我們要注意安全，讓我們感受到即便離鄉背井到台北讀書也能擁有額外的溫暖。

再者感謝我的家人們，從小到大扶持我、使我能夠衣食無憂地生活以致能夠專心準備每個人生階段大大小小的考試與考驗；也感謝周遭的親朋好友們，即便人生至此走的道路不盡相同，卻還是能在需要的時候出現、照顧彼此，好度過一些充滿壓力的時期；還有實驗室一起奮鬥的同儕、學弟妹、學長，多虧有學長們良好的經驗傳承，在自己獨當一面進行研究時才能夠順順利利；幸好有學弟妹的幫忙，可以讓我免除心力去勞煩一些繁瑣的事。

最後要感謝的是我自己，人生總是有奮鬥不完的階段，二十多年一直以來即便偶有鬆懈、怠惰、氣餒之時，你總是能夠適時調整回良好的狀態，繼續為了自己期許的目標拚搏，期許接下來的你也能夠維持著這樣的心態，盡全力面對接下來的每一個挑戰。

doi:10.6342/NTU202404706

目次

doi:10.6342/NTU202404706

doi:10.6342/NTU202404706

圖次

doi:10.6342/NTU202404706

doi:10.6342/NTU202404706

doi:10.6342/NTU202404706

doi:10.6342/NTU202404706

doi:10.6342/NTU202404706

doi:10.6342/NTU202404706

Chapter 1 Introduction

1.1 Introduction of Light Amplification by Stimulated Emission of Radiation (LASER)

Speaking of laser, it always comes with stimulated emission, which was proposed by Albert Einstein in 1916[2]. Few years after, Charles H. Townes and Arthur Schawlow worked out the concept of optical maser, the word known as Microwave Amplification by Stimulated Emission of Radiation [3], published by *Physical Review* in 1958. Gordon Gould was the person who coined the term LASER, which stands for Light Amplification by the Stimulated Emission of Radiation within his notes then filed a patent application in 1959, yet it was not until 1987 that the officials finally granted the patent to him. The first ever functioning laser was made by Theodore Maiman, using ruby crystal, on the day of May 16, 1960. In the following years, gas and semiconductor lasers were carried out, and the former has usually been used in the fields such as welding metals and medical surgeries for its high-power characteristics, while the semiconductor lasers back then weren't as useful as nowadays comparing to for it requiring pulsed operation and low temperature.

doi:10.6342/NTU202404706

As for the DFB laser we especially concern in this topic, H. Kogelnik and C. V. Shank in 1970, the first team to discover the behavior of stimulated emission oscillating inside periodic structures, saying its resonator composed of spatial periodic variation of refractive index rather than mirrors, resulting in the feedback from backward Bragg scattering[4].

Later in the 1980s, thanks to the huge progress in semiconductor fabricating process, semiconductor lasers finally overcame its disadvantages so that it could lower the threshold current, operate with continuous wave, work under room temperature, broaden its emitting wavelength, and functioning as single-mode, which is crucial in optical communications.

The applications of laser have become widespread and has played a big role in our daily lives nowadays. For instance, optical communications with fiber[5] or satellite[6] communications, light detection and ranging as LiDAR[7], high accuracy sculpting, medical uses such as skin rejuvenation and eye surgery[8], military[9], and still among others.

doi:10.6342/NTU202404706

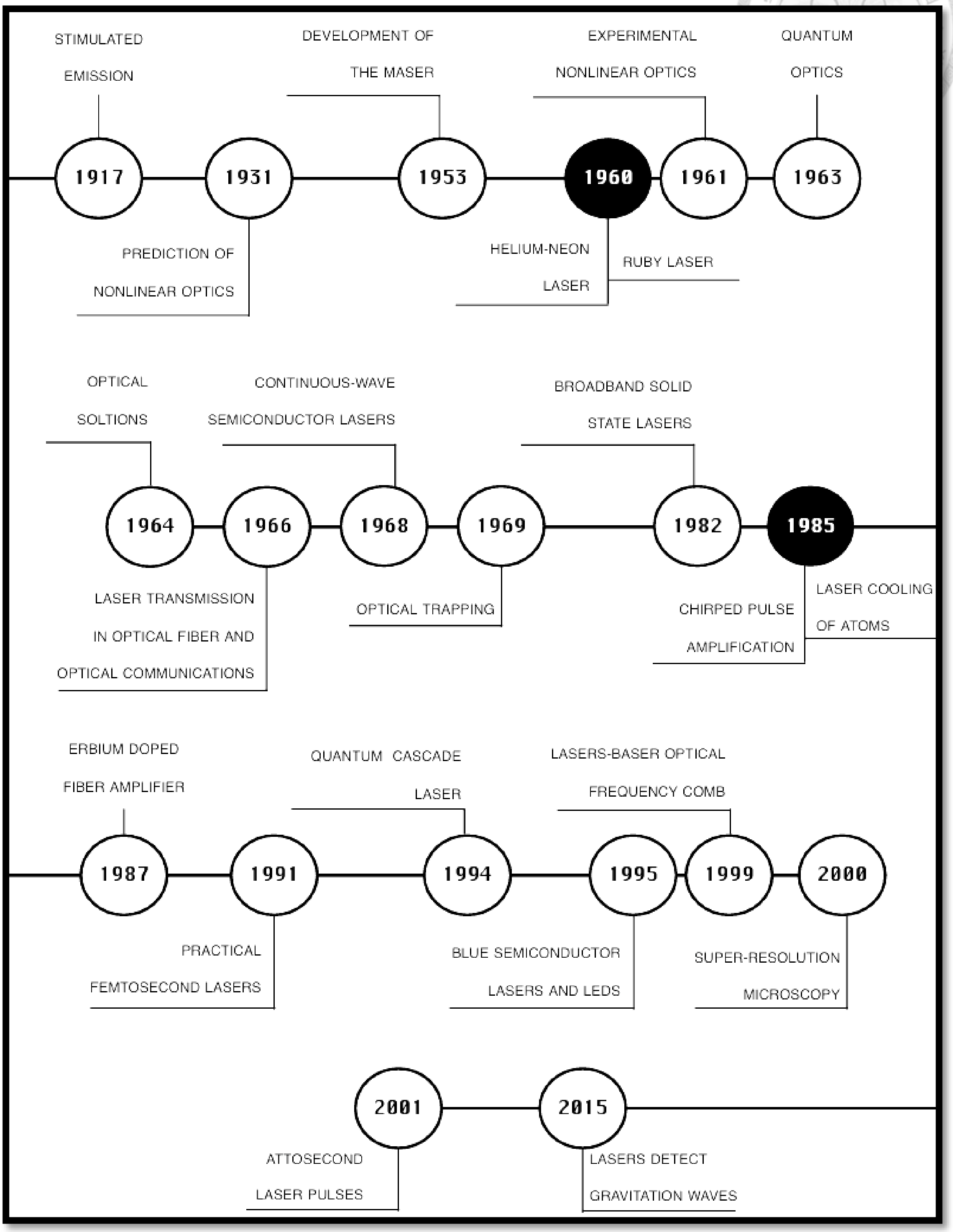

Figure 1 The development of laser [10].

doi:10.6342/NTU202404706

1.2 Motivation

Although traditional lasers can achieve high power and single-mode output, it is difficult to attain both at once. For example, vertical-cavity surface-emitting lasers (VCSELs), can function in single longitudinal mode but struggle to attain high power output for the small gain medium volume in their short-length resonant cavities[11]. On the contrary, traditional edge-emitting lasers (EELs), such as Fabry-Perot (FP) lasers, can achieve high power (from milliwatts to watts) from their larger resonant cavity length and gain medium volume, however, conventional FP lasers only provide multimode output [12], which is not preferred in long-range communications. As for distributed feedback (DFB) lasers, with its Bragg gratings designed along the waveguide near the active layer, allowing them to select specific wavelengths for feedback, which enables single-mode output, ensuring that signals remain undistorted over long-distance transmission while maintaining a relatively high output power[13].

The practical application projects involving DFB lasers as a light source such as LiDAR, silicon-based photonic devices, and ground-satellite communications, require the unique characteristics of narrow bandwidth, single-mode output, and high power. Ideally, the power should enhance as the cavity length is increased. Therefore, in this

doi:10.6342/NTU202404706

study, we aim to achieve high power output by fabricating long-length resonant cavities then observe the effects on power and spectral distribution under various lengths and widths of the resonant cavities.

1.3 Operational principles of a DFB Laser

1.3.1 Basic structures of a laser

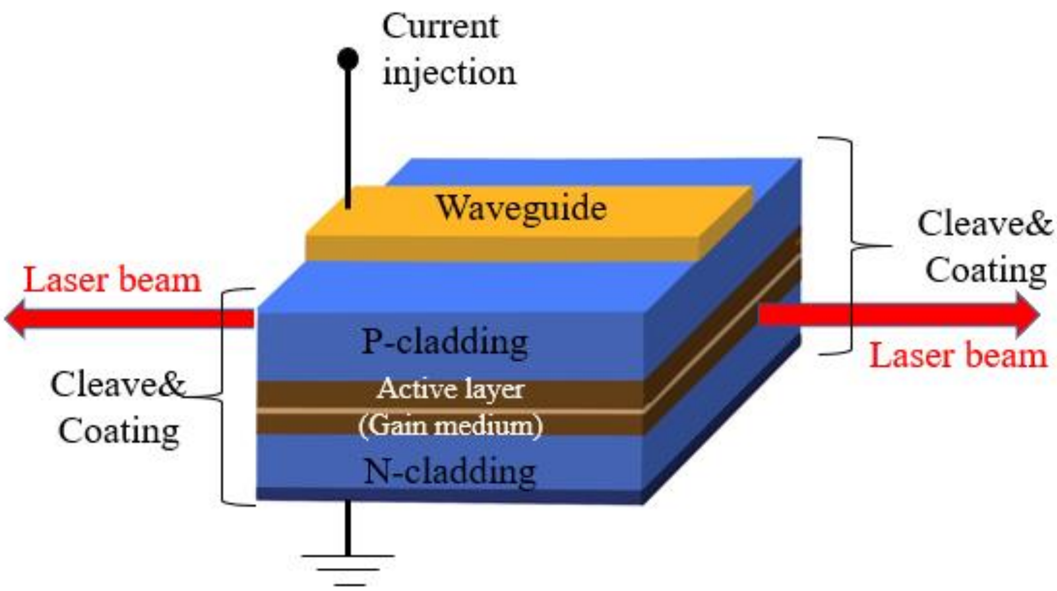

Figure 2 The basic structures of an edge emitting semiconductor laser

The basic structures of a semiconductor laser are mainly composed of gain medium, pump source, resonant cavity. The active layer is viewed as the gain medium, whereas to achieve the condition of population inversion and is grown between p and n-type cladding layers in an edge emitting laser, as shown in **Figure 2** The basic

doi:10.6342/NTU202404706

structures of an edge emitting semiconductor laser. When apply a forward-biased voltage on this p-n junction, electrons and holes, as the pump source, recombine for both non-radiative and radiative emission in which latter generates photons from spontaneous and stimulated emission. However, its is spontaneous emission that occurs when start injecting minority electrons and holes. To acquire the population inversion for stimulated emission’s dominance, it is crucial to introduce in the resonant cavity as the mechanism of mirror in order to reflect and keep photons inside cavity, together with the increase of injections, the optical gain can thus finally overcome the scattering, free carrier absorption[14], inertial loss, and the mirror loss in the cavity. **Equation 1** shows that it is not only but reaching the threshold gain so the device lases at steady state[15]. Even if carriers continue to be injected into the active layer, the gain coefficient will no longer increase. When the gain exceeds the loss, the light within the resonant cavity will be amplified continuously, leading to instability. As a result, the excess carriers will be converted into coherent photons, producing laser output.

$$\gamma_{th} = \alpha_i + \frac{1}{2L} ln\left(\frac{1}{R_1 R_2}\right) \qquad \textbf{Equation 1}$$

γ_{th}: $Threshold\ gain;$ α_i: $Internal\ loss$

L: $Cavity\ length$

doi:10.6342/NTU202404706

$R_1 \& R_2: Reflectivities\ of\ two\ sides\ of\ cavity$

$$\frac{1}{2L} ln\left(\frac{1}{R_1 R_2}\right): Mirror\ loss$$

The critical point between spontaneous and stimulated emission is referred to as the threshold current when plot the light-current (L-I) curve like **Figure 3**. Ideally when driving a laser from low to high current gradually, it emits photons randomly as a light emitting diode (LED) by spontaneous emission before turning into a laser with the mechanism of stimulated emission, providing characteristics of coherence, monochromaticity, and directionality.

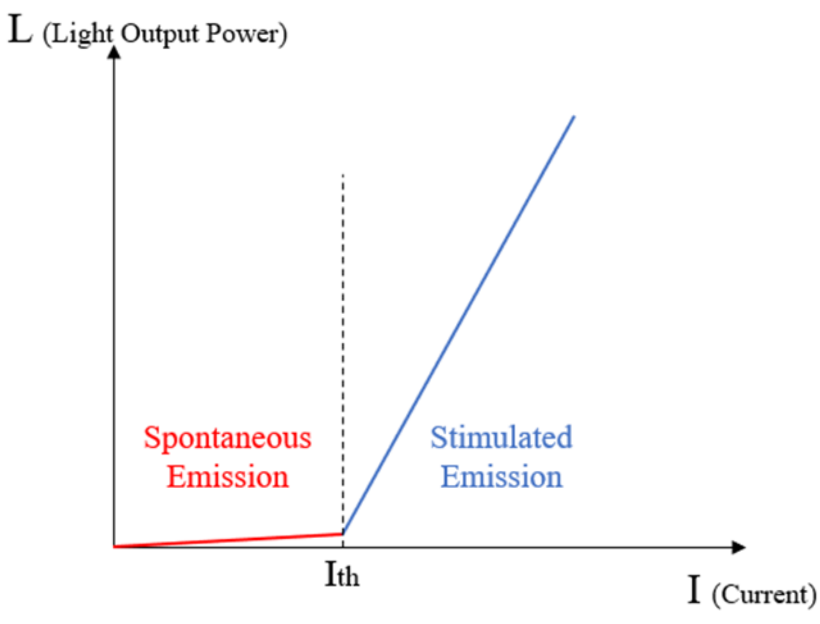

Figure 3 The light-current curve of a laser diode

doi:10.6342/NTU202404706

1.3.2 Basic concepts of a Distributed Feedback (DFB) laser

A DFB (Distributed Feedback) laser achieves mode selection by fabricating a grating-like periodic structure along the resonant cavity near the active layer. This provides different feedback mechanisms for various longitudinal modes. For two counter-propagating waves to be coherently coupled within the cavity, the Bragg condition below as **Equation 2** should be satisfied[16]. This ensures that the feedback is maximized on both sides of the Bragg wavelength.

$$\Lambda = m\frac{\lambda_0}{2n_{eff}}\ , m = 1,2,3\ ... \quad \textbf{Equation 2}$$

$$\Lambda: Grating\ period;\quad n_{eff}: Refractive\ index\ of\ the\ cavity$$

$$m: Number\ of\ diffraction\ order;\ \lambda_0: Laser's\ wavelength\ in\ freespace$$

However, the grating structure alone cannot achieve single-mode operation[17], it is more like double mode as shown in **Figure 4(a)**. One of many methods is that by coating both ends of the resonant cavity with anti-reflection (AR) and high-reflection (HR) mirrors[18], which reflectivity is related to wavelength, the original two-mode symmetry could be disrupted, and enabling such single-mode operation in **Figure 4(b)**.

doi:10.6342/NTU202404706

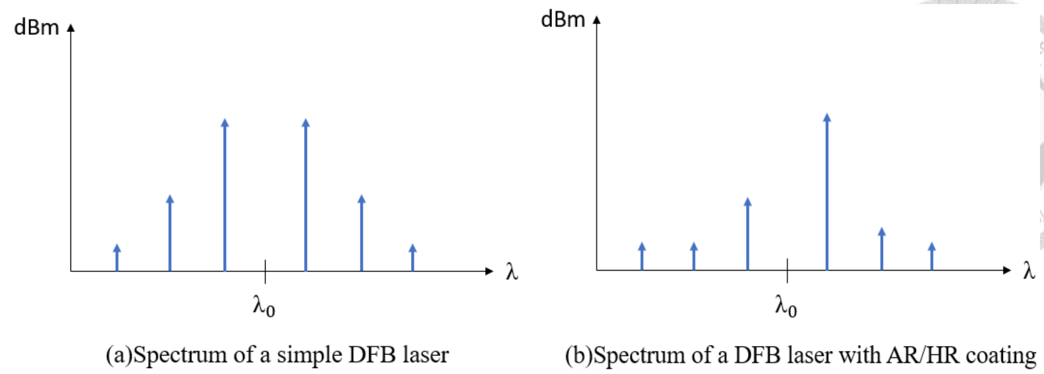

Figure 4 (a) Spectrum of a simple DFB laser **(b)**Spectrum of a DFB laser with AR/HR coating

1.4 Review of previous papers

As many laboratories have dug into the related topics of DFB laser, recently it is the Silicon Photonics that rises the further development in the high-power semiconductor lasers[19]. Broadcom [20] illustrated that high-power laser play a crucial role in silicon photonics for maintenance of signal integrity, high-speed communication, and functionalities despite loss from the Silicon-based waveguide coupling.

In 2019, Hao Wang and Ruikang Zhang fabricated a 1.5μm DFB laser with a highest power of 160mW under room temperature (25°C) and with the side mode suppression ratio (SMSR) of 55dB [21], shown in **Figure 5**.

doi:10.6342/NTU202404706

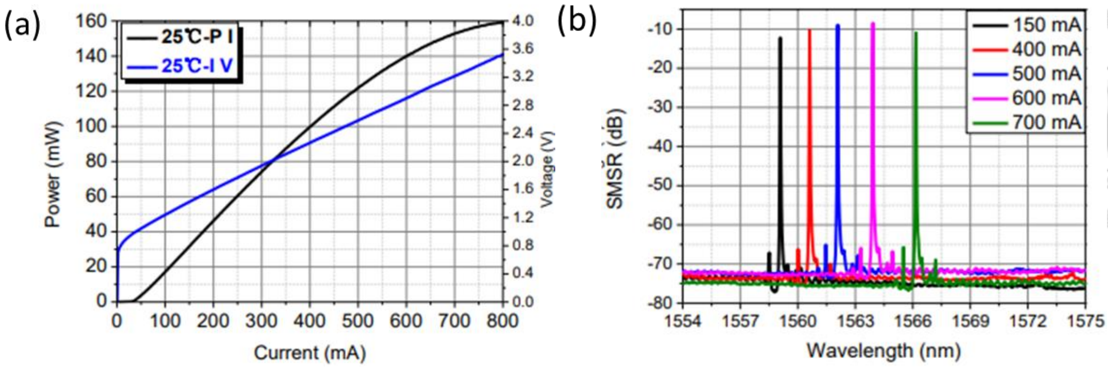

Figure 5 (a)The L-I-V characteristics under room temperature (25°C) with a highest power of 160mW (b) The spectra under various input currents (at 25°C), and the SMSR is up to 55 dB [21].

The next year, O.O. Bagaeva and R.R. Galiev published a paper of an experimental study on 1.5-1.6μm high-power single-frequency semiconductor DFB lasers, with a highest power of 200mW and SMSR around 55dB [22], shown in **Figure 6**.

doi:10.6342/NTU202404706

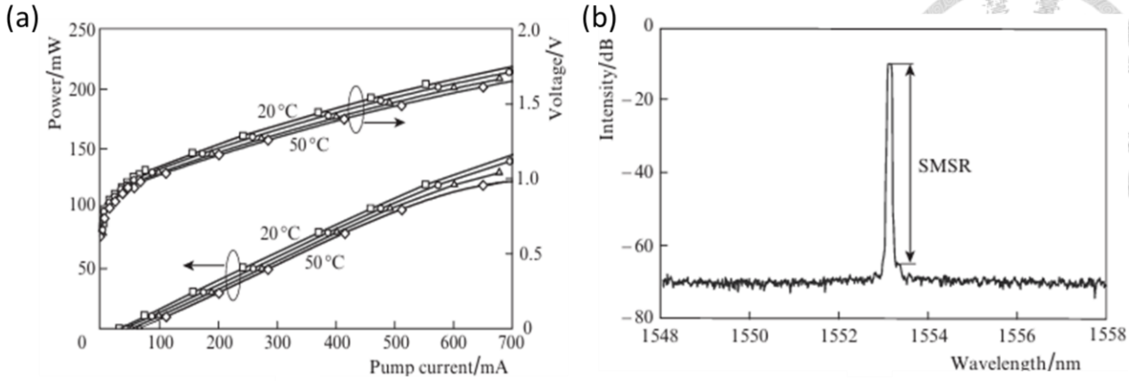

Figure 6 (a) I-V and L-I characteristics of DFB lasers for temperatures of 20, 30, 40, and 50 °C, with a highest power of 200mW (b) Spectra of the DFB laser at a pump current of 500 mA, with the SMSR about 55dB [22].

Later in 2021, Huawei Technologies published a paper for record-high power 1550nm DFB laser[23], having output power over 700mW with a cavity length of 2mm. The next year[24], pretty much the same team made a DFB laser that can achieve 800mW at room temperature and yet still reach 600mW at 55°C with a cavity length of 2.5 mm instead of the previous one for higher output power to be saturated. Performances of the lasers in two researches mentioned above are illustrated in **Figure 7**.

doi:10.6342/NTU202404706

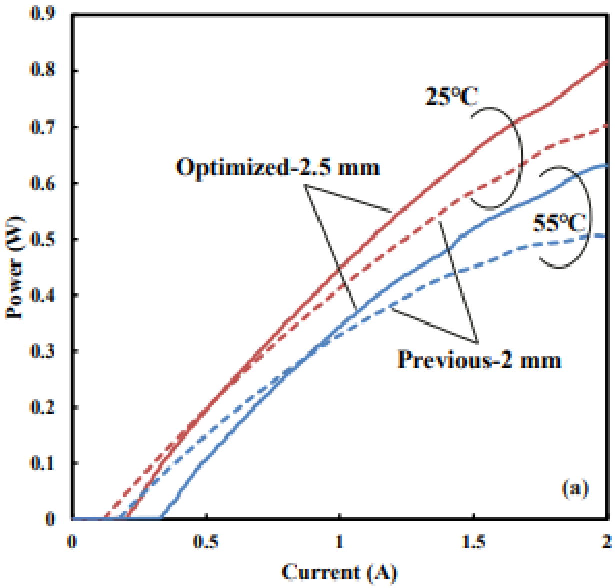

Figure 7 L-I curves comparison between 2mm and 2.5mm cavity length DFB lasers[24]

Through the literature review above, we understand the role of high-power lasers and its current progress in this field. The article written by Osamu Mikami 1981 Jpn. J. Appl. Phys. 20 L488 [25] , serves as a reference for our fabrication methods. This paper employs wet etching to create the wanted structure, subsequently using Si_3N_4 as a mask to open and deposit metal contacts. The P-metal is composed of nickel-zinc alloy, while the N-metal is made of nickel-germanium alloy. Last but not least, a cleaving process is carried out on the front facet and cutting the rear one by wire saw to avoid Fabry-Perot-alike modes.

doi:10.6342/NTU202404706

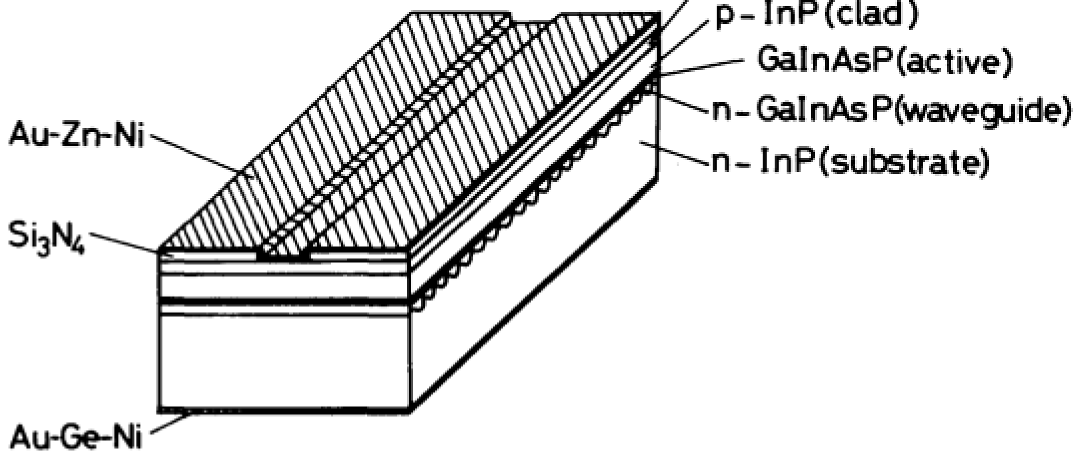

Figure 8 Illustration of a InGaAsP/ InP DFB laser[25]

However, different from the wet etching applied to the former paper, we adopted the method which is introduced in 2003 [26],of inductively coupled plasma etching (ICP) to fabricate our ridge-shaped waveguide such as **Figure 9**, for the small-sized ridge structure to be intact and unharmed.

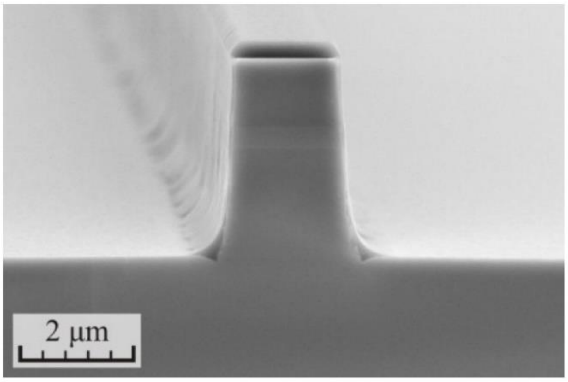

Figure 9 SEM image for cross-section of the ridge waveguide[26]

doi:10.6342/NTU202404706

Chapter2 Instruments and Principles for Process

2.1 Photolithography Process

Photolithography is indispensable when it comes to the semiconductor component fabrication for it determines the shape and structure of further processes. It involves designing mask for the pattern, defining the geometric shapes of photoresists by applying exposure and development, allowing the designed pattern to be transferred onto the wafer.

Photoresist is a photosensitive material and is generally categorized into positive and negative resist. Positive photoresist becomes soluble in a developer solution after experiencing the UV light exposure through a mask and leaves the pattern of the unexposed regions after development. In contrast, negative photoresist hardens upon exposure and remains after development, defining the patterned areas. With the exposure, areas not exposed to UV light dissolve during development, leaving a pattern of the regions exposed. Positive photoresist offers higher resolution, making it ideal for applications requiring smaller feature sizes and finer details. In contrast, negative photoresist is commonly used before coating metals for it creates undercut profiles after development, making the removal of excess material easier in the subsequent lift-off

doi:10.6342/NTU202404706

processes. **Figure 10** shows the difference in both photoresists. To sum up, both photoresists play essential roles in modern photolithography, with positive one commonly used in advanced semiconductor manufacturing and the negative one preferred for certain metallization and patterning techniques.

Furthermore, the thickness and uniformity of the photoresist depends on the parameters of spinning speed and time during the spin coating process. Moreover, different photoresists have varying stickiness and characteristics, allowing them to be used in different situations.

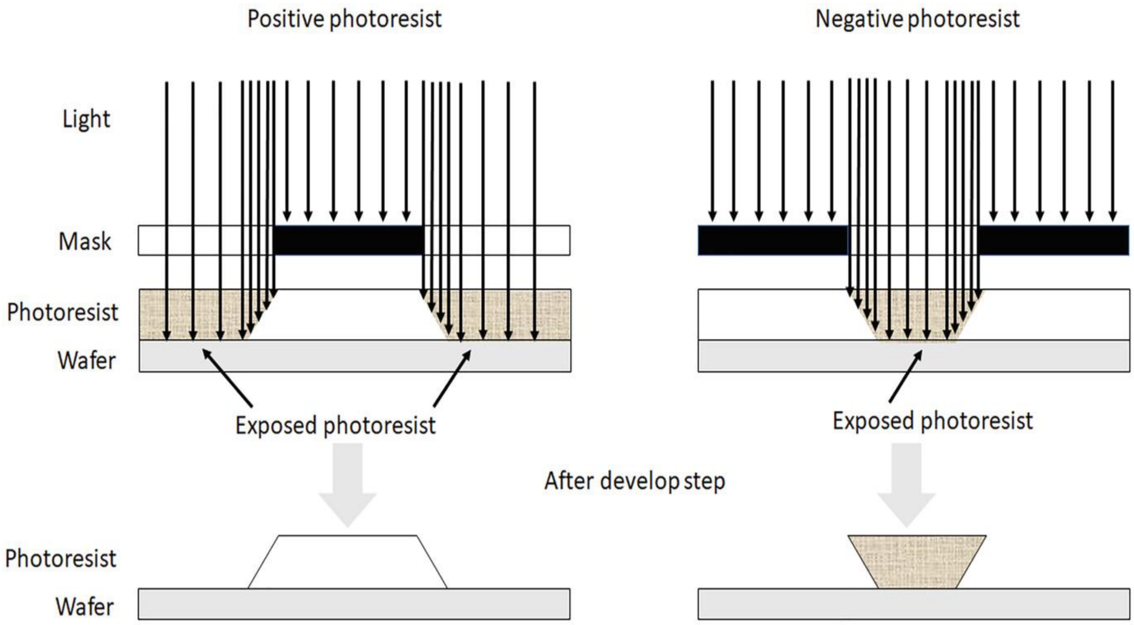

Figure 10 Profiles of positive and negative photoresist[27]

The general steps for the photolithography process during our experiment are listed below as:

doi:10.6342/NTU202404706

1. *Wafer and photomask preparation*: Rinse with acetone, isopropyl alcohol, and deionized water for the removing of possible contaminants or particles on them that could lead to defects after processes.

2. *Spin coating*: First we apply hexamethyldisilazane (HMDS) to the wafer for a better adhesion between photoresist, which would be coated on later.

3. *Soft bake*: Performed on a hot plate 90 second at 105°C, ensuring the solvents that may remain on the surface to evaporate, increasing the adhesion of the photoresist to substrate, and yielding for a stable pattern after exposure and development.

4. *Exposure*: Align the wafer with the photomask then expose it with UV light, defining the shape of the pattern. Parameters of exposure time and light power along with the developing time are crucial for the quality of pattern.

5. *Development*: Dipping the substrate into developer solution to dissolve places where the photoresists were exposed before if positive photoresist was used. Rinse the substrate with deionized water right after the expected patterns emerge to prevent overdevelopment. On the contrary, the use of negative

doi:10.6342/NTU202404706

photoresist would have the unexposed places to be dissolved. The controlling of developing time is vital for the quality of the pattern.

2.2 Plasma Enhanced Chemical Vapor Deposition (PECVD) for Film Protection

Plasma Enhanced Chemical Vapor Deposition (PECVD) is a technique used to deposit thin films by utilizing plasma to drive chemical reactions at lower temperatures compared to conventional CVD methods. In this process, gases containing reactive precursors, such as silane (SiH_4) or ammonia (NH_3), are introduced into a vacuum chamber, where an RF or microwave power source generates plasma from the gas mixture. The plasma enhances the reactivity of the gas molecules, enabling film formation on the substrate surface at temperatures typically between 100°C and 400°C [28]. Therefore, such technique is ideal for applications involving temperature-sensitive materials.

PECVD is commonly implemented to form silicon-based films such as silicon nitride (Si_3N_4) and silicon dioxide (SiO_2), which are widely used in microelectronics, MEMS, and optoelectric devices, their chemical reaction equations are shown below as

doi:10.6342/NTU202404706

Equation 3 and **Equation 4**, respectively. The deposition technique provides benefits of uniform film coverage, precise control over thickness, and low intrinsic stress, which are essential for passivation layers and insulating coatings. Key parameters such as gas flow rate, RF power, pressure, and temperature can be fine-tuned to modify the film's properties, including density, mechanical stress, and refractive index, to suit specific requirements.

$$3\ SiH_4(g)+2\ NH_3(g)\rightarrow Si_3N_4(s)+6\ H_2(g) \qquad \textbf{Equation 3}$$

$$SiH_4(g)+2\ O_2(g)\rightarrow SiO_2(s)+2\ H_2(g) \qquad \textbf{Equation 4}$$

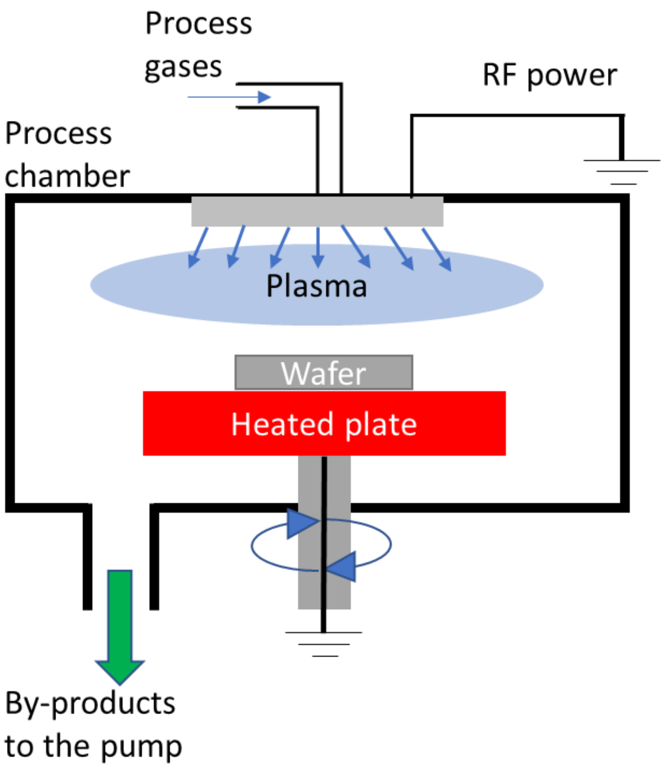

Figure 11 Schematic illustration of a conventional PECVD reactor[29]

doi:10.6342/NTU202404706

2.3 Etching Process

Etching is a crucial process in microelectronics and semiconductor fabrication for the use of selectively remove materials to create patterns or structures as designed. It is generally divided into dry and wet etching. Dry etching utilizes gases or plasma in a vacuum chamber, providing high precision through anisotropic etching, where material is removed primarily in one direction to achieve well-defined vertical sidewalls. Common gases include fluorine- and chlorine-based compounds, depending on the material being processed. Techniques such as Reactive Ion Etching (RIE) and Inductively Coupled Plasma (ICP) are widely used for example. On the other hand, wet etching involves immersing the material in a chemical solution that reacts with the surface to dissolve unwanted areas. Wet etching tends to be isotropic, meaning it etches uniformly in all directions, which could be unexpected of small patterns but is effective for processes that require large etching area and high etching rates. Both methods play crucial roles in modern semiconductor manufacturing, with dry etching favored for precision and wet etching for high-throughput needs.

doi:10.6342/NTU202404706

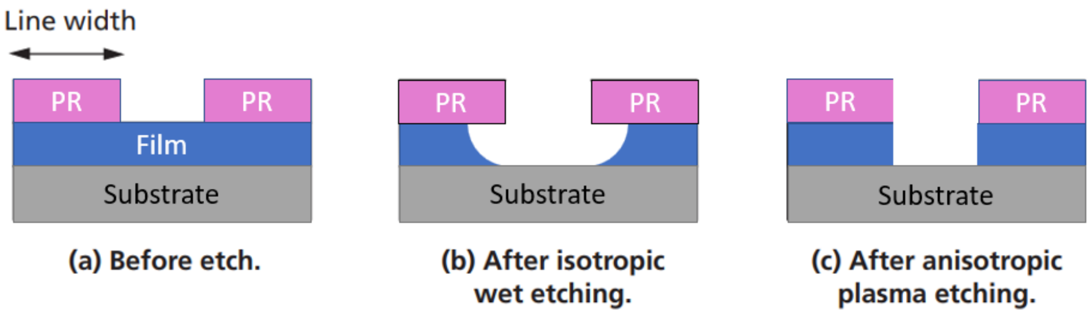

Figure 12 Schematic presentation of the dry and wet etching.[30]

2.4 Self-Aligned Technique

In microfabrication of semiconductor, self-aligned processes can be applied to open contacts without needs of precise manual alignment, thus minimizes misalignment that may be caused by human or the linewidth limit due to diffractions. **Figure 13** shows the general steps of the self-aligned technique applied to a ridge waveguide for the further metal contact[31].

doi:10.6342/NTU202404706

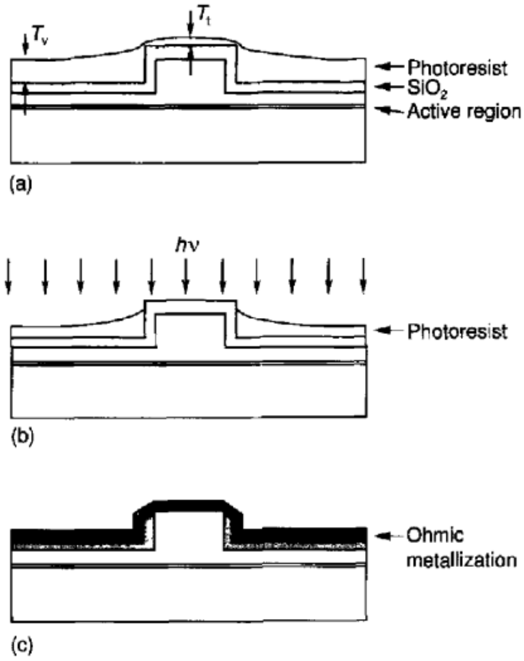

Figure 13 Schematic illustration of the self-aligned technique: (a)Spin coating the photoresist onto the wafer (b) Developing after exposure (c)Open-contacted with ohmic metallization[31]

2.5 Ohmic Contact

Ohmic contact allows current to flow in both directions between the metal and semiconductor, following a linear relationship with voltage as described by Ohm's law (I = V/R), ensuring no rectifying behavior from Schottky contact occurs. A key advantage of this type of contact is its low resistance, which helps minimize energy loss and supports the efficient operation of high-performance devices such as lasers, which we especially concern. Achieving optimal Ohmic contact depends on precise material

doi:10.6342/NTU202404706

selection and manufacturing processes. Metals need to be chosen to match the semiconductor's properties to reduce resistance. For instance, nickel (Ni) or gold (Au) are often used with p-type semiconductors, while n-type semiconductors may utilize a nickel-germanium-gold (Ni-Ge-Au) alloy. Additionally, masking layers like Si_3N_4 or SiO_2 are employed during fabrication to confine metal deposition to specific areas, avoiding short circuits. Proper implementation of these steps ensures reliable low-resistance contact, and is crucial for devices requiring high efficiency.

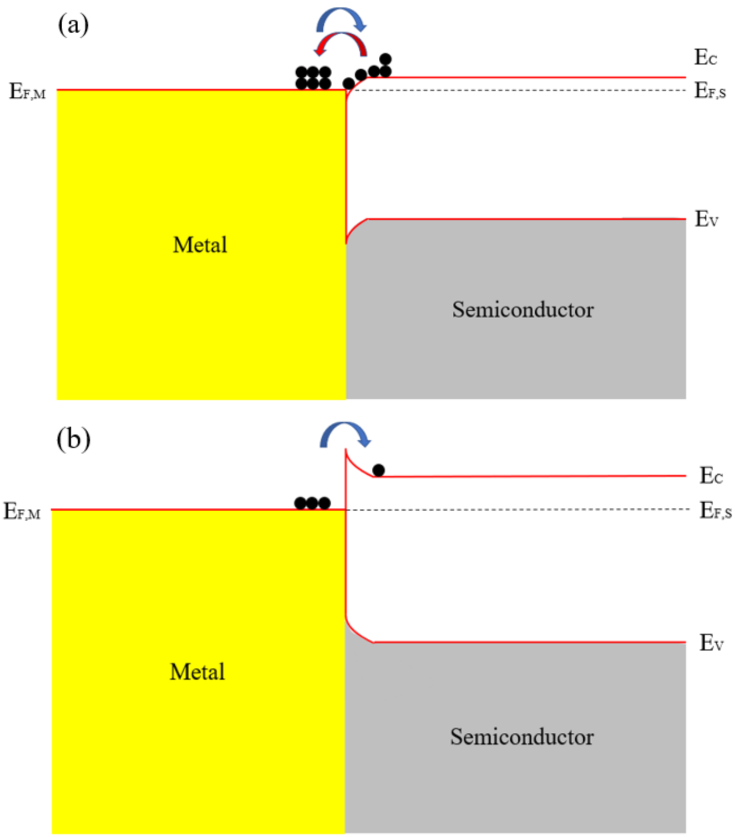

Figure 14 (a) Ohmic and **(b)** Schottky contact

doi:10.6342/NTU202404706

2.6 Electron Beam (Gun) Evaporation for Metal Deposition

E-gun, also referred to as E-beam deposition, involves directing a focused electron beam onto a target material to heat until it evaporates, forming a thin film on wafer. This process takes place in a vacuum chamber to prevent oxidation and contamination, ensuring high-purity layers. Metals like gold and nickel are often used, with gold providing excellent conductivity and corrosion resistance, and nickel enhancing adhesion or serving as an ohmic contact layer. E-beam deposition has its advantages in offering precise control over film thickness and uniformity, making a high quality in metal contact for semiconductor components.

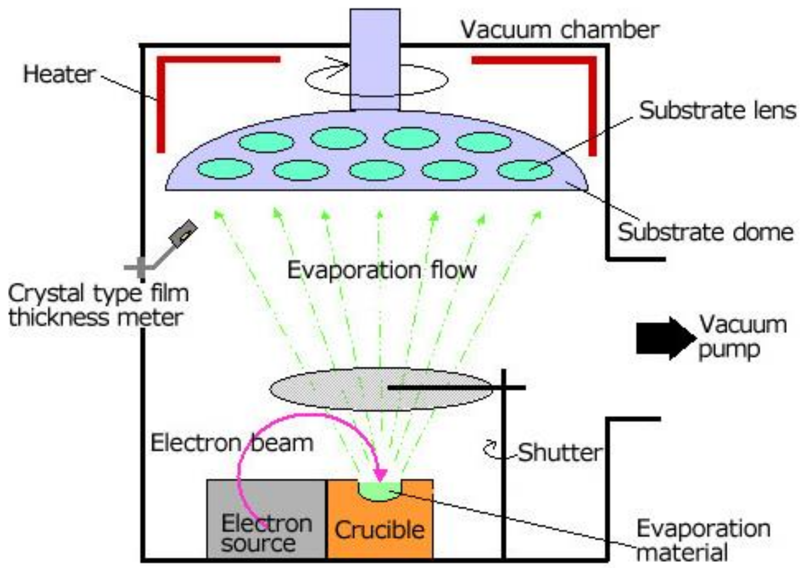

Figure 15 An electron beam evaporation device from JEOL[32].

doi:10.6342/NTU202404706

Chapter3 Device and Process Flow Design

3.1 A Simple View of the Device Structure

In this study, we have two slightly different versions of the device structures. The first was fabricated in-house in the school's cleanroom, while the second was fully outsourced to *Union Optronics Corporation* for manufacturing with our process designs. **Figure 16** shows the one fabricated by ourself is designed with **(a)**circle and **(b)**square p-metal pads connected to the short cavities such as 300 and 500μm while the long cavities of 750 and 1250μm attached to **(c)**rectangle pads with the hope that the current could spread uniformly through the longer ridges. The passivation layer was chosen for Si_3N_4, expecting for a stronger protection than SiO_2.

doi:10.6342/NTU202404706

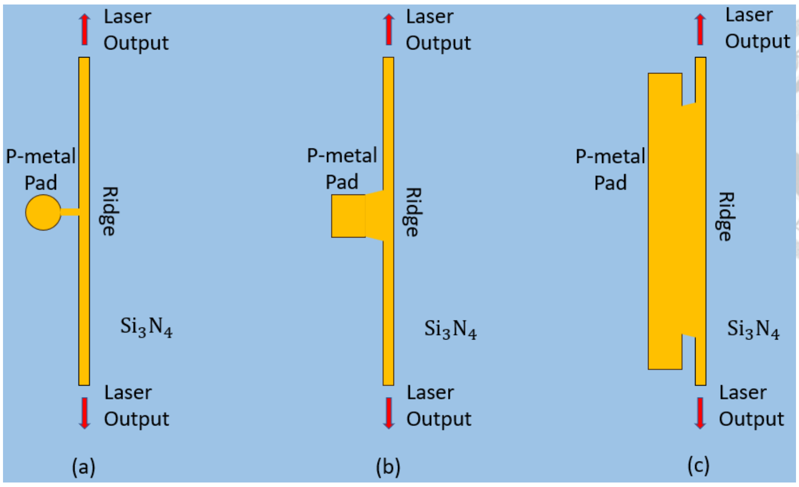

Figure 16 Schematic illustration of **(a)** Circle **(b)** Square **(c)** Rectangle p-metal pads of the device structure fabricated in-house

As for the version outsourced, the instruments were believed to be more stable and promising, so the layer passivated on wafer as SiO_2 should be protecting well enough. Moreover, the chemical plating was implemented right after the p-metal process so the connection between metal pad and ridge are fine for current spreading, so the metal pads of long cavities are circles and squares rather than the rectangle ones we mentioned above.

doi:10.6342/NTU202404706

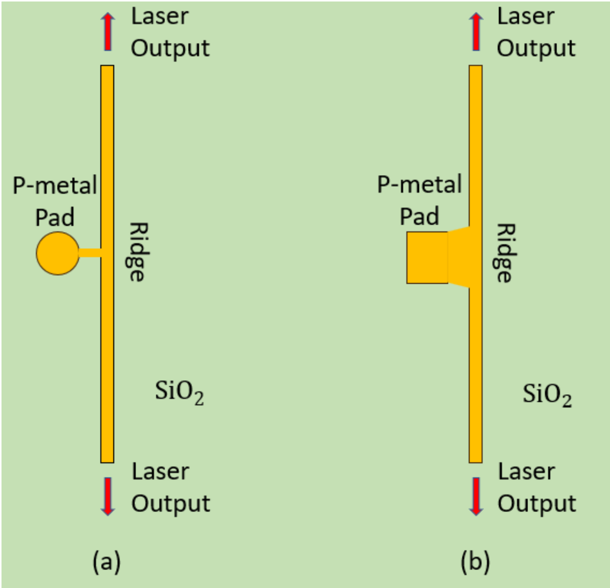

Figure 17 The metal pads for devices of the outsourced version are circles and squares all over different cavity lengths

doi:10.6342/NTU202404706

3.2 Process Flow of Fabrication

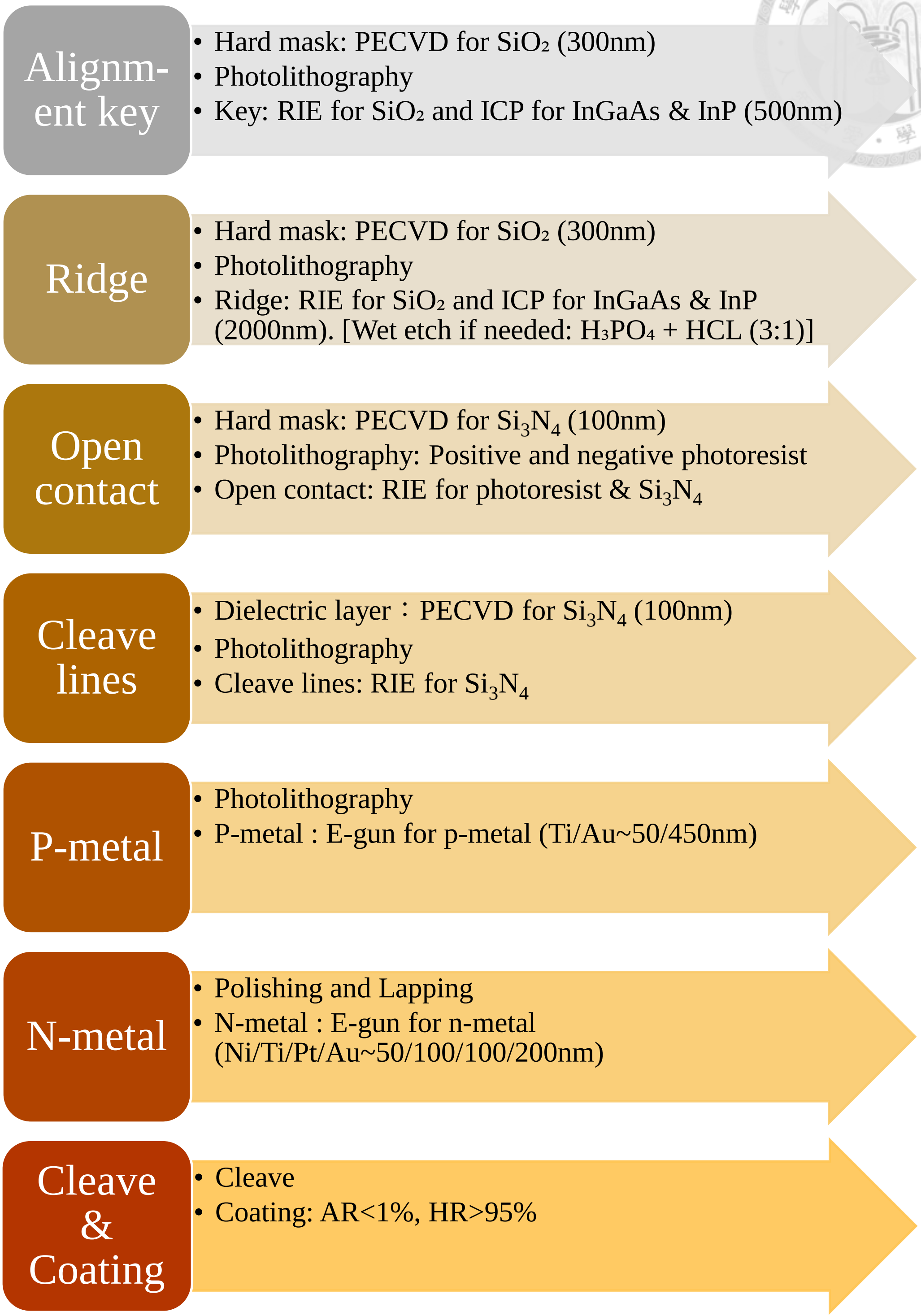

Figure 18 The procedure of the fabrication on DFB laser wafer

doi:10.6342/NTU202404706

3.2.1 Alignment key

In the very first step, SiO_2 is deposited as a hard mask of 300nm using Plasma Enhanced Chemical Vapor Deposition (PECVD). Next, a positive photoresist, AZ5214, is applied using a spin coater, then the alignment key pattern is defined through exposure and development along the direction of the grating structure. Subsequently, Reactive Ion Etching (RIE) and Inductively Coupled Plasma (ICP) are used to etch downwards of the surrounding areas of the key for the thickness of 300nm and 500nm in SiO_2 and InGaAs/ InP, respectively. Finally, acetone and Buffered Oxide Etch (BOE) are used for the removal of photoresist and SiO_2, resulting in the structure of the key, which is for the further alignment of the following processes.

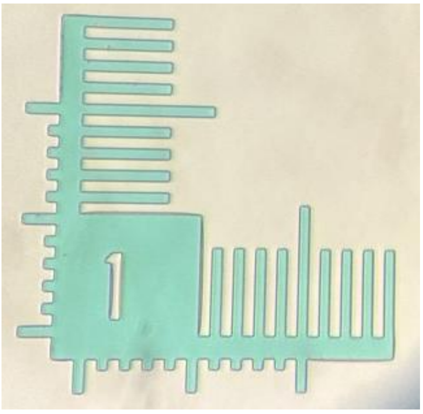

Figure 19 The alignment key observed under optical microscope

doi:10.6342/NTU202404706

3.2.2 Ridge Etching

For the ridge structure, the process step is pretty similar to the former key etching. As shown in **Figure 20(a)**, we deposited SiO_2 for the hard mask in advance, implemented photoresist AZ5214 for the photolithography, **(b)**etched down the hard mask with RIE and clean up the photoresist with acetone, **(c)**then perform a further etch of InGaAs& InP with ICP. Lastly, **(d)**remove the residual SiO_2 with BOE.

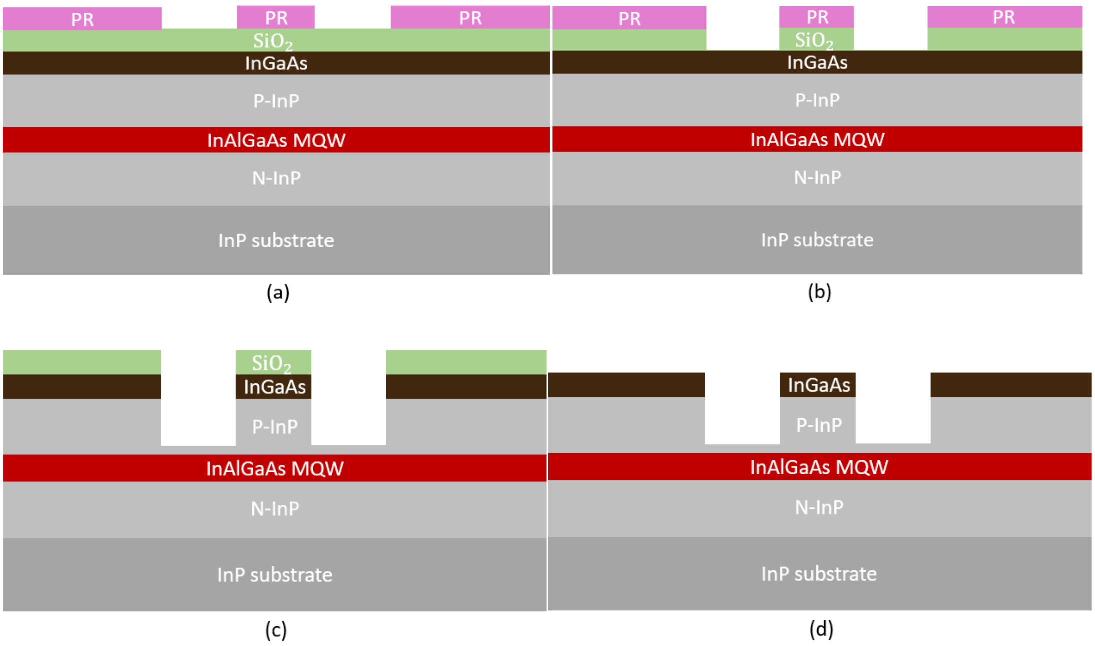

Figure 20 (a) Deposited SiO_2 and performed photolithography for AZ5214 **(b)** Hard mask etching with RIE **(c)** A further etch of InGaAs& InP with ICP **(d)** Remove the residual SiO_2 with BOE

doi:10.6342/NTU202404706

3.2.3 Open contact and Cleave lines

In the open contact and cleave lines process shown as **Figure 21**, **(a)** we chose Si_3N_4 as the hard mask and passivation layer for further protection, it is deposited with PECVD. For the photolithography parts, **(b)** we first apply a layer of photoresist AZ5214 through a flood exposure along with reverse bake [33] thus the resist is converted to be as negative photoresist. Subsequently, an additional layer of AZ5214 photoresist is applied, forming a dual-layer resist system for self-alignment purposes. **(c)** Upon exposing and developing, the remaining resist on the ridge would be the negative one only. Next, we apply RIE to **(d)** remove the resist on ridge until it was completely etched away, while leaving photoresist in other areas only partially removed. Still with RIE, **(e)** the layer of Si_3N_4 above ridge would be etched completely for the open contact. Last but not least, **(f)** the residual photoresist is removed with acetone, leaving the surfaces out of the top of the ridge to be remained with protection of Si_3N_4 layer.

doi:10.6342/NTU202404706

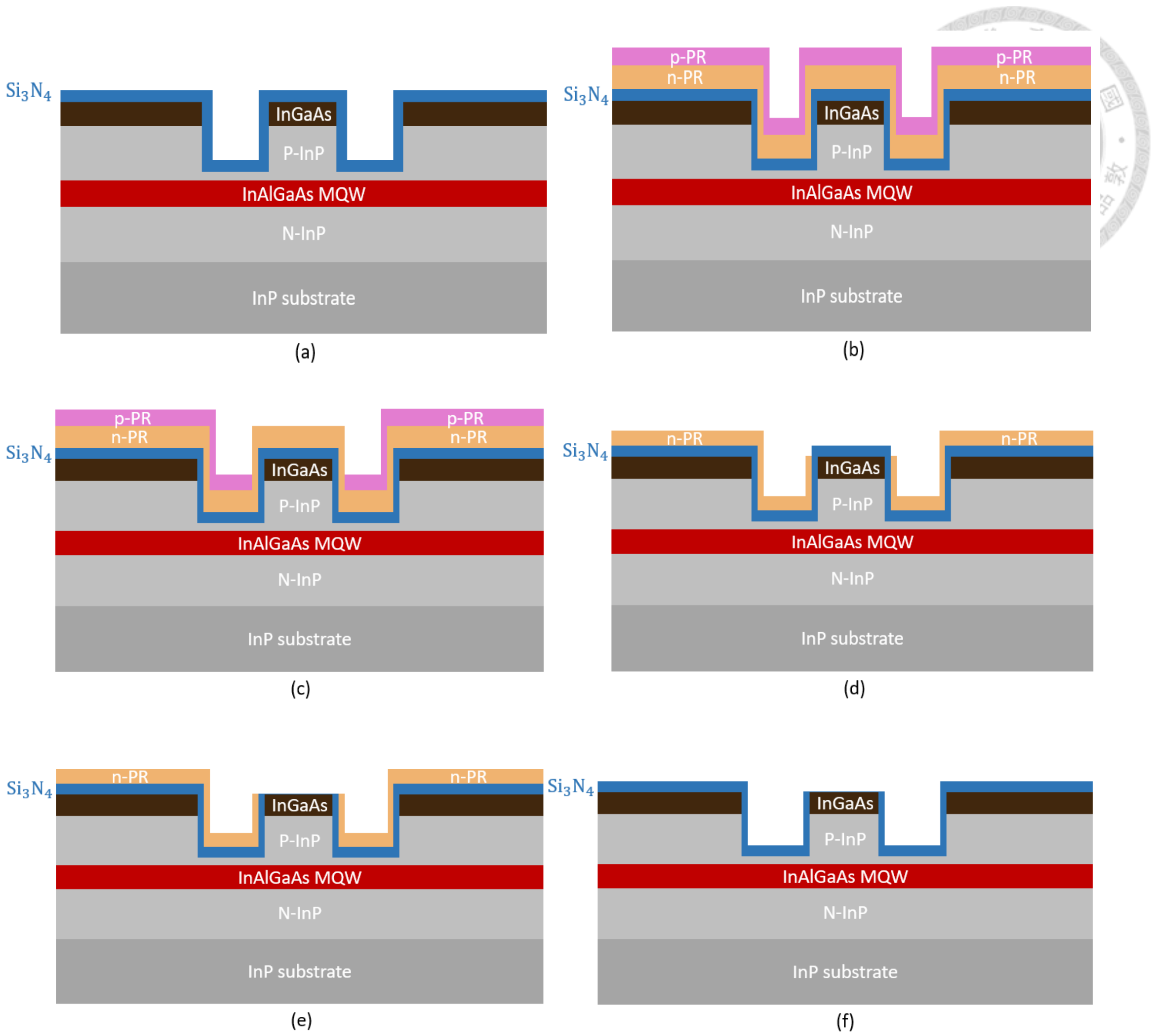

Figure 21 Process for open contact and cleaving lines: **(a)** Deposit Si_3N_4 as the hard mask and passivation layer **(b)** Dual-layer resist system for self-alignment purposes **(c)** During photolithography, the remaining resist on the ridge would be the negative one only**(d)** Removing the resist on ridge with RIE **(e)** The layer of Si_3N_4 above ridge be etched completely **(f)** The residual photoresist is removed with acetone

The reason for utilizing the self-aligned technique is that the linewidth of the photomask could not be sized to 2μm, which is the minimum width of the ridge. Also,

doi:10.6342/NTU202404706

it is more promising for not requiring precise alignment that could be mistaken during the manual operation by human.

3.2.4 P-metal & N-metal

After opening the passivation layer above the ridge, we apply the negative photoresist to define the pattern for the p-metal for its undercut profile benefits the lift-off process. The sputtered metals via E-gun are titanium (Ti) and gold (Au), with thicknesses of 50 nm and 450 nm, respectively, in a total of approximately 500 nm, as **Figure 22** shows. The titanium serves as an adhesion layer, while gold provides excellent conductivity.

Similarly, the backside was coated with n-metal after lapping and polishing to a total thickness about 120μm, which is for the cleaving process later on, an alloy of Ni/Ti/Pt/Au with 50/100/100/200 nm, respectively, where Ni provides adhesion to the semiconductor, Ti enhances adhesion and acts as a diffusion barrier, Pt prevents gold diffusion and maintains electrical properties, and Au ensures excellent conductivity and corrosion resistance, ensuring stable electrical contact and long-term reliability.

doi:10.6342/NTU202404706

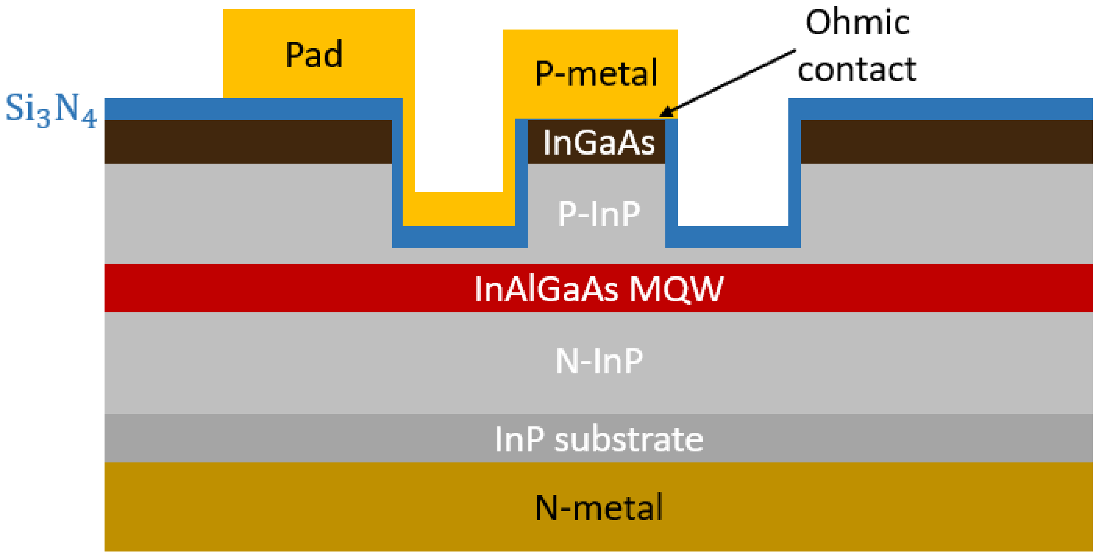

Figure 22 P, N-metal for Ohmic contact along with lapping& polishing

3.2.5 Cleaving and Coating

Both cleaving and coating were outsourced to *LandMark Optoelectronics Corporation* since the there is no relevant equipment available in-house. The cleaving process help to divide each laser row on the wafer fabricated into laser bars as shown in **Figure 23 (a), (b)**. Moreover, this process is essential for shaping device facets as mirrors, to achieve optimal optical performance.

doi:10.6342/NTU202404706

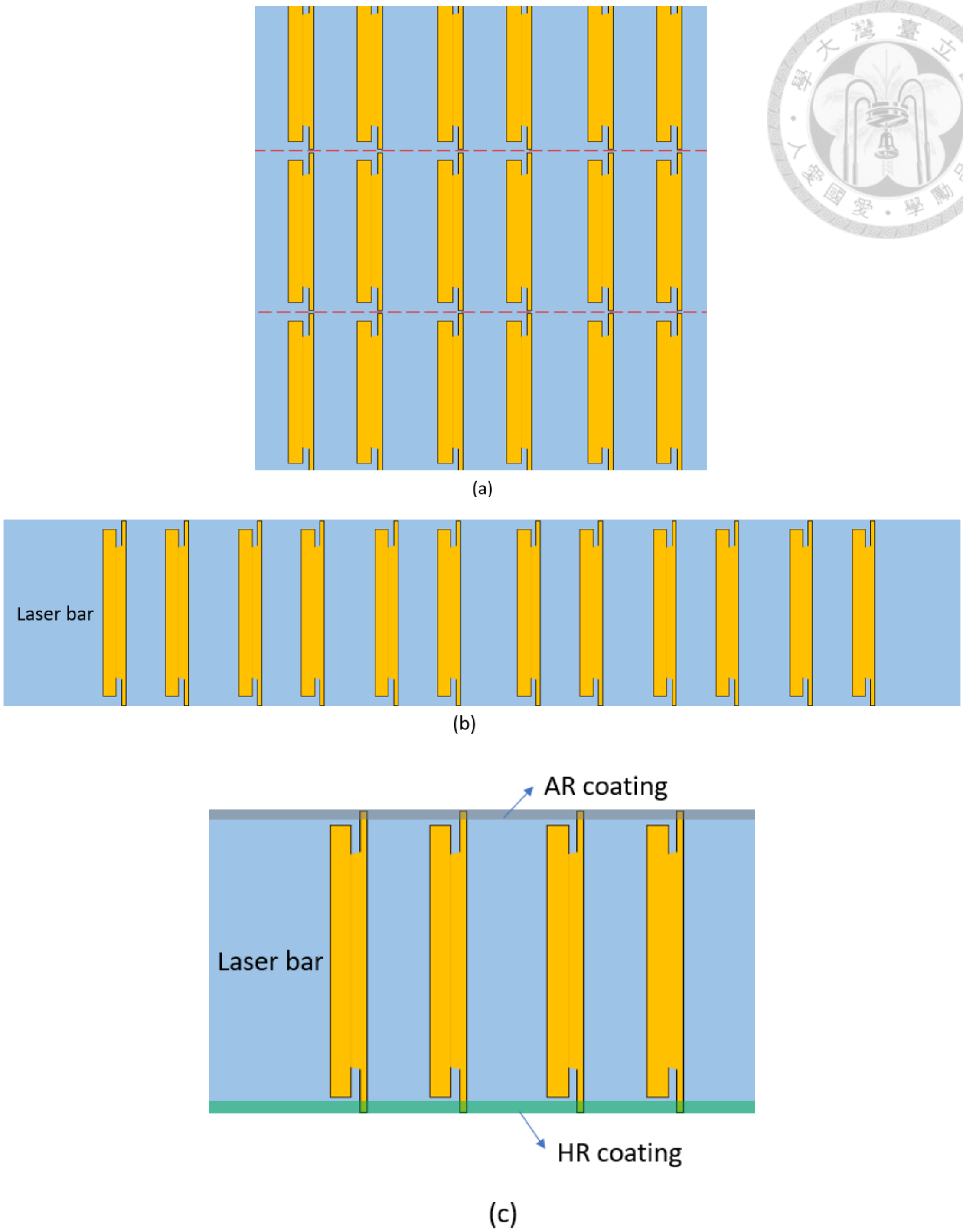

Figure 23 (a) The red dashed-line stands for the cleaving line **(b)** Several laser bars would be separated from the wafer **(c)** Anti and high-reflective coating on both cleaved ends

doi:10.6342/NTU202404706

Finally, shown in **Figure 23 (c),** the last step is thin film deposition on both sides of the cleaved edges, with the conditions being that the AR (Anti-Reflective) coating on the output surface should be less than 1%, and the HR (High-Reflective) coating should be greater than 95%. Thin film coatings on laser components play essential roles in enhancing performance. AR coatings reduce the amount of light that is reflected away from the output surface, which improves the transmission of laser light and boosts overall efficiency. HR coatings, used on mirrors inside the laser cavity, reflect more than 95% of the light, which increases both intensity and output power. Moreover, these coatings can be specifically designed for certain wavelengths, leading to optimized laser output. They also protect the components from environmental influences such as oxidations, contributing to their durability and longevity.

Chapter4 Electrical and Optical Analysis

4.1 Electrical Properties of DFB Lasers

Here we compare the I-V characteristic in log scale of the in-house (clean-room #R331) and UOC fabricated laser devices under same size, shown below in **Figure 24**.

doi:10.6342/NTU202404706

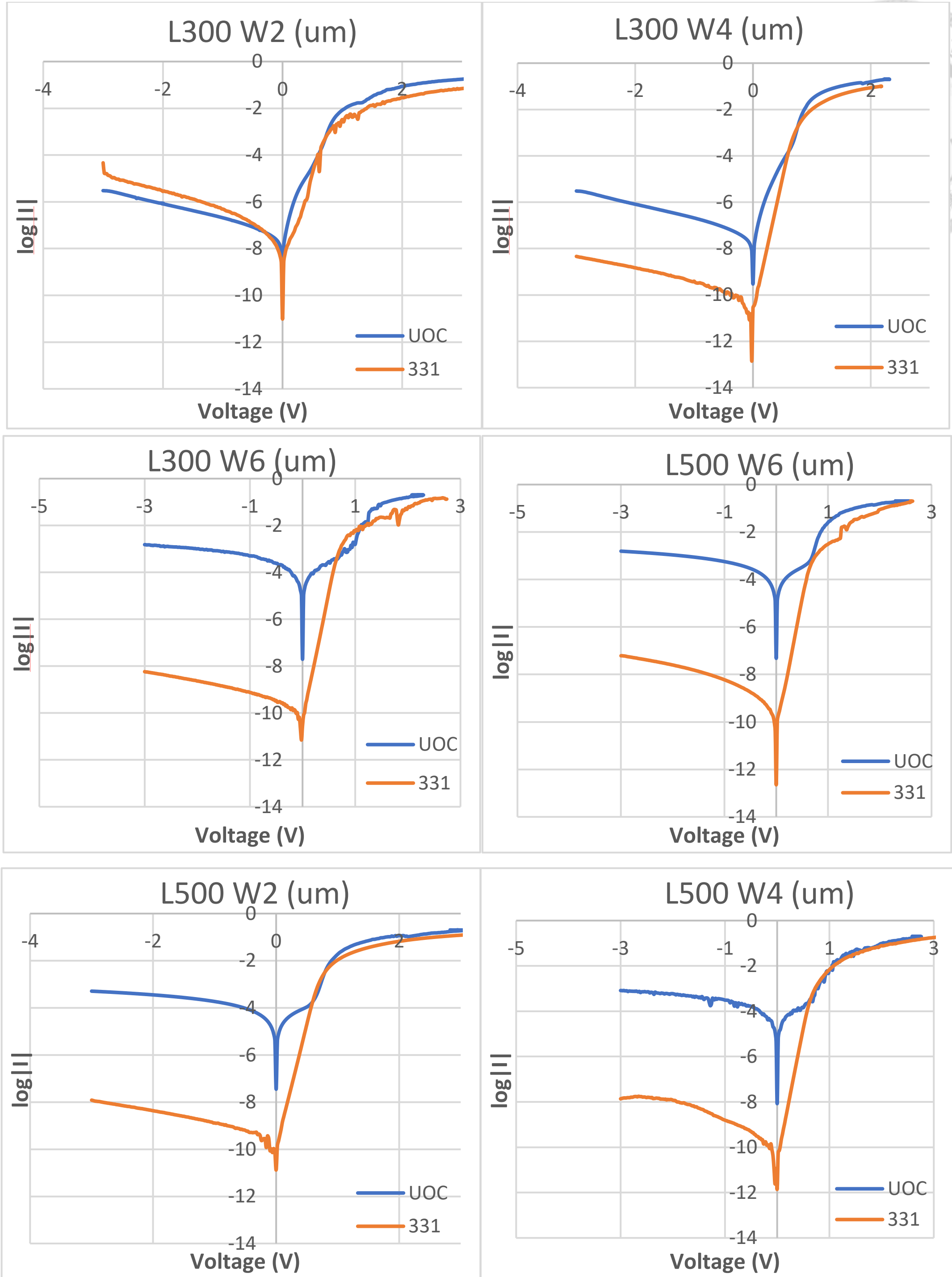

doi:10.6342/NTU202404706

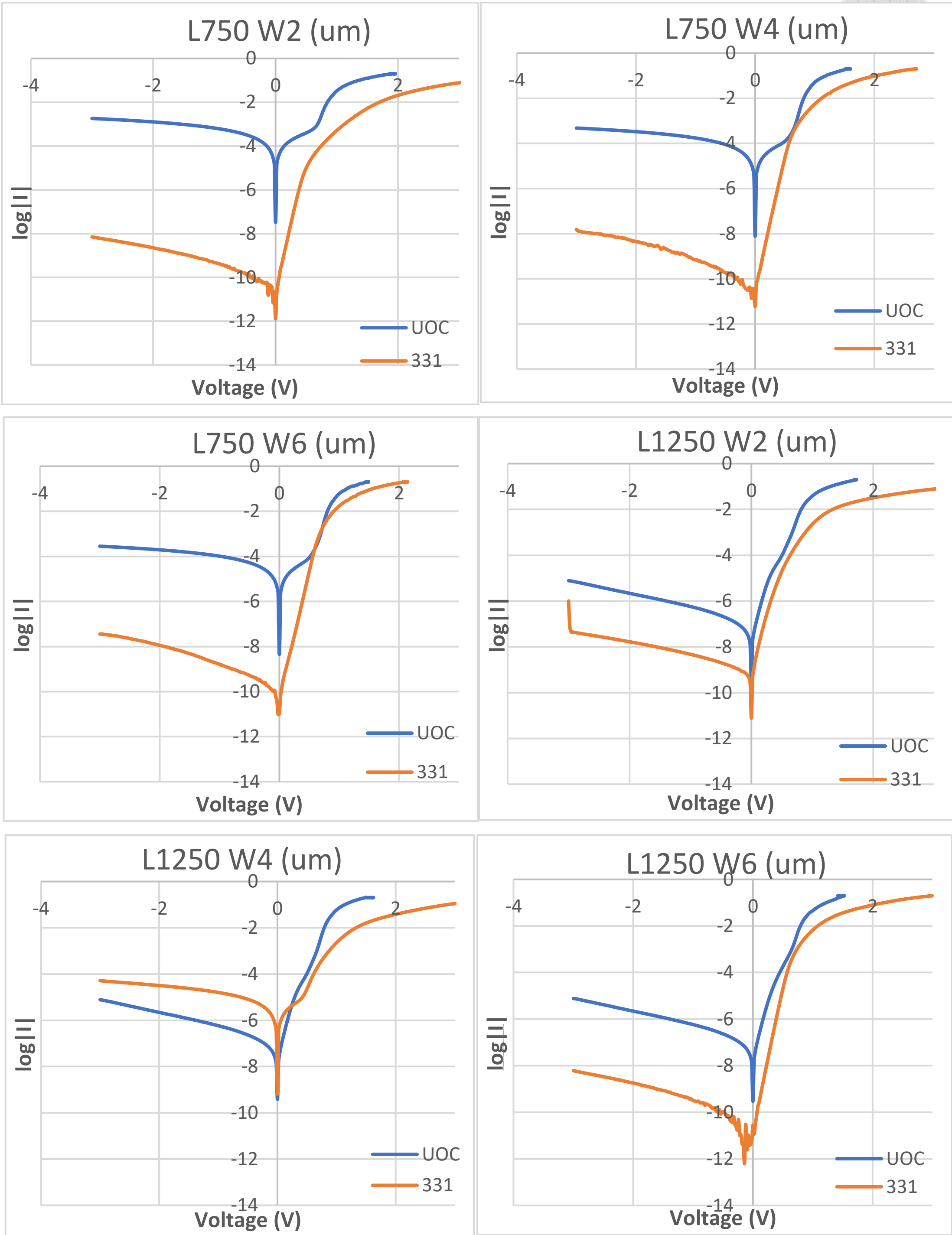

Figure 24 I-V characteristic comparison in log scale of in-house and UOC fabricated laser devices under same size. To distinguish between different geometries of the lasers, L750 means 750-micron cavity, and W2 means 2-micron ridge width.

doi:10.6342/NTU202404706

4.1.1 Shunt Resistance Rp

As shown above, most of the UOC devices present a 3-section between 0~1V while R331 devices don't. For a brief explanation, we could take into account the equivalent circuit model of a diode with shunt (Rp) and series (Rs) resistance, shown as **Figure 25** [34]. According to the previous log I-V comparison, it is Rp that dominates the log I-V curve in the section of 0V to 0.7V. Also based on **Figure 25(d)**, **Figure 26** illustrates the R331 components do not exhibit a turning point because the shunt resistance (Rp) is relatively high (resulting in a lower slope), leading to a smaller current. As a result, the entire curve shifts downward, aligning closely with the original red dashed line of the diode, resembling a straight line.

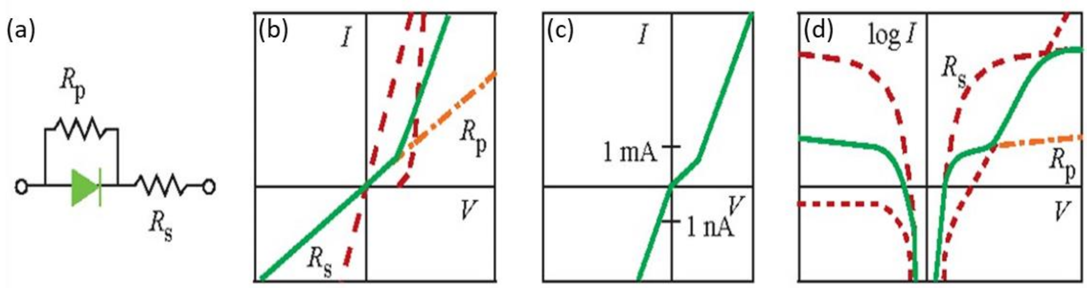

Figure 25 Equivalent circuit model of a diode with shunt and series resistance. The green solid line represents the actual measured I-V data of the laser diode while red and orange dashed-line stand for Rs and Rp, respectively[34].

doi:10.6342/NTU202404706

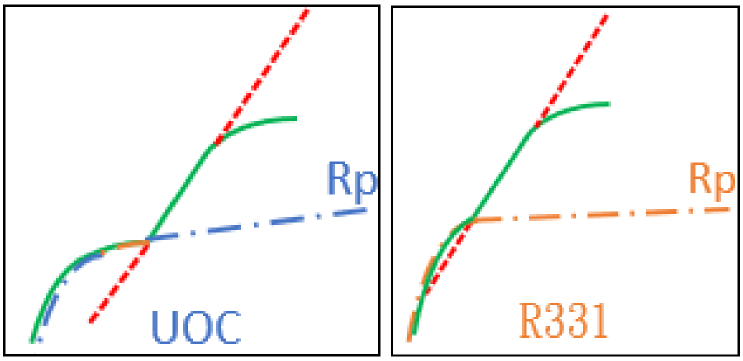

Figure 26 The R331 component (the graph on the right) does not exhibit a turning point because Rp is relatively high resulting in a lower slope and a smaller current. As a result, the entire curve shifts downward, aligning closely with the original red dashed line of the diode

4.1.2 Ideality Factor n

Typically, the ideality factor n of a semiconductor device falls within the range of 1 to 2. However, as shown in **Figure 27**, one device has reached a maximum of 4.7 (4.678), while some are above 2. For several factors, such as defects on the surface, and the metal contact fracture from the poor depositing quality, could lead to non-radiative combination and heat. Moreover, the shunt resistance we mentioned above also played an important role in resulting in a higher ideality factor than 2.

doi:10.6342/NTU202404706

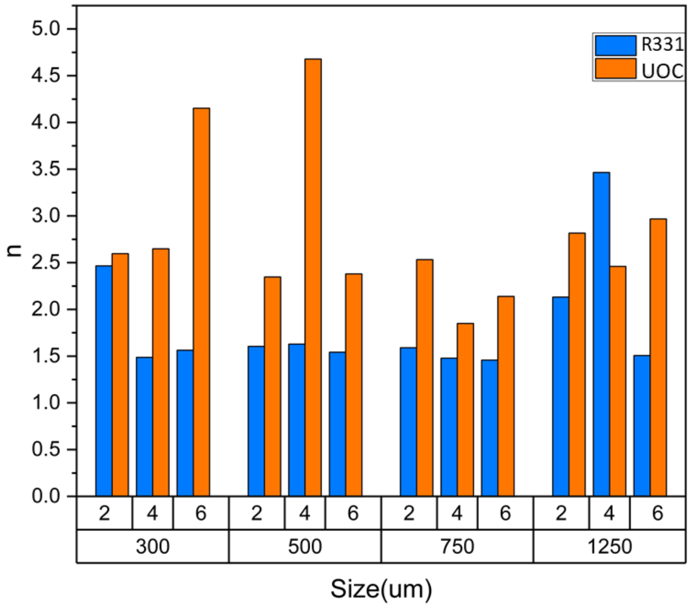

Figure 27 The ideality factor n of the R331& UOC devices in each size

The ideality factor data is acquired from the ln|I|-V plot we measured. Combining with **Equation 6**, which is derived from diode's current equation, **Equation 5**, we have the slope $m = \frac{\Delta lnI}{\Delta V}$ and Ideality factor $n = \frac{1}{m}\frac{qV}{kT}$ of the linear section as shown in **Figure 28**. Note that the ideality factor's acquisition of R331 devices might not be accurate because the presence of the shunt resistance is strong and no turning point is observed as in the UOC devices.

$$I = I_0\left(exp\left(\frac{qV}{nkT}\right) - 1\right) \qquad \textbf{Equation 5}$$

$$ln\, I = ln\, I_0 + \frac{q}{nkT}V \qquad \textbf{Equation 6}$$

doi:10.6342/NTU202404706

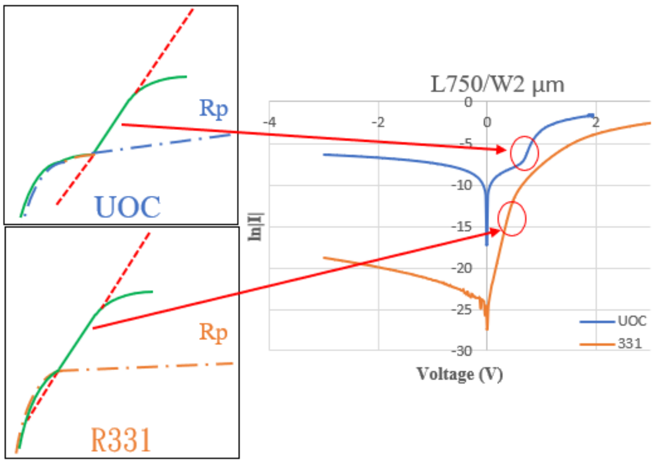

Figure 28 Linear section of ln|I|-V plot for the ideality factor n acquisition.

4.1.3 Series Resistance Rs

Series resistance refers to the resistance that is in series with the laser diode of the circuit. The resistance leads to a voltage drop that could affect the overall efficiency and performance of the device.

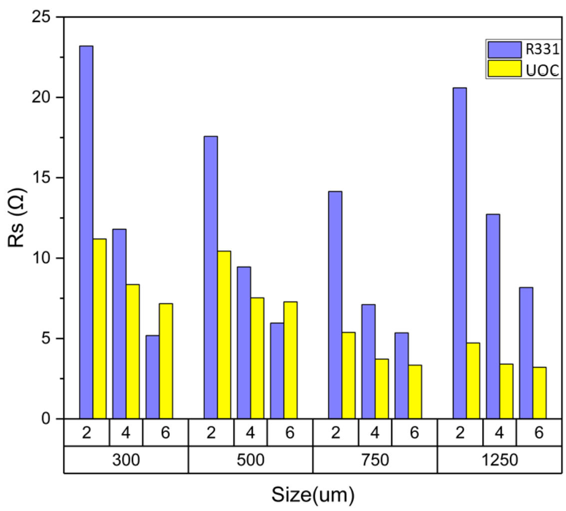

Figure 29 The series resistance Rs of devices in each size for both R331 and UOC devices

doi:10.6342/NTU202404706

It is seen that in **Figure 29**, R331 devices' resistance are commonly larger than that of UOC's. The difference might be caused by the defects on the metal contact surface, or the addition of metal plating after metal contacting in UOC's process.

4.2 Optical Properties of DFB lasers

4.2.1 L-I Characteristic of the DFB lasers

Here we presented several L-I (Light Power-Current) characteristic charts of the devices in comparison with different width and length.

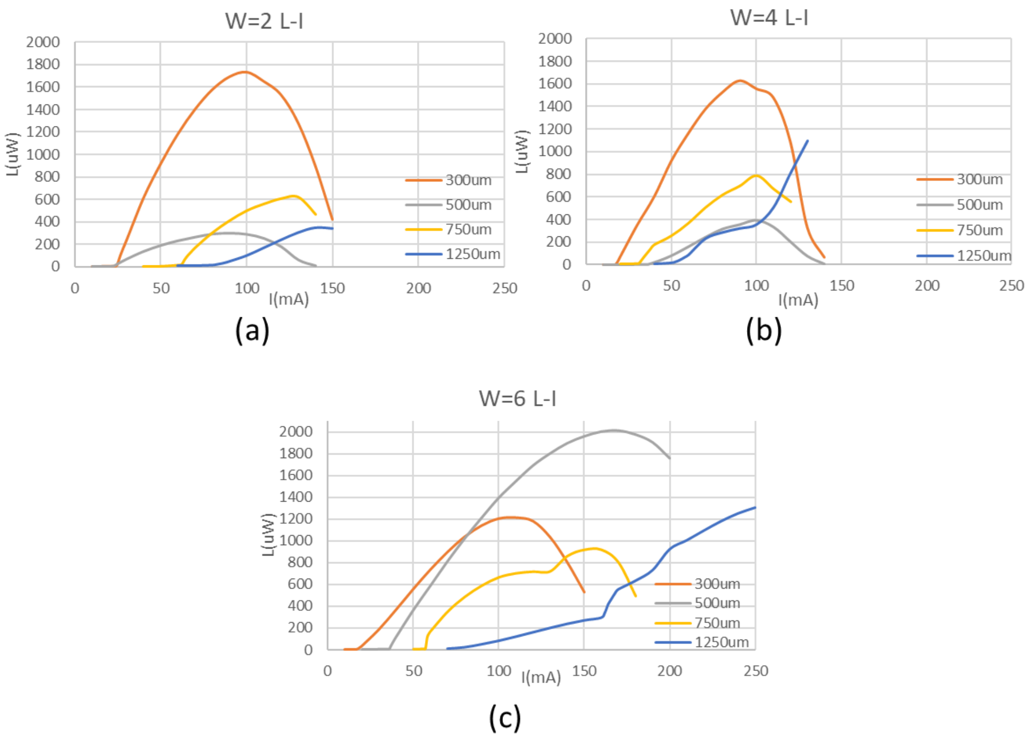

Figure 30 L-I characteristics comparison of R331 devices of various cavity lengths with (a) ridge width= 2μm; (b)ridge width= 4μm; (c)ridge width= 6μm.

doi:10.6342/NTU202404706

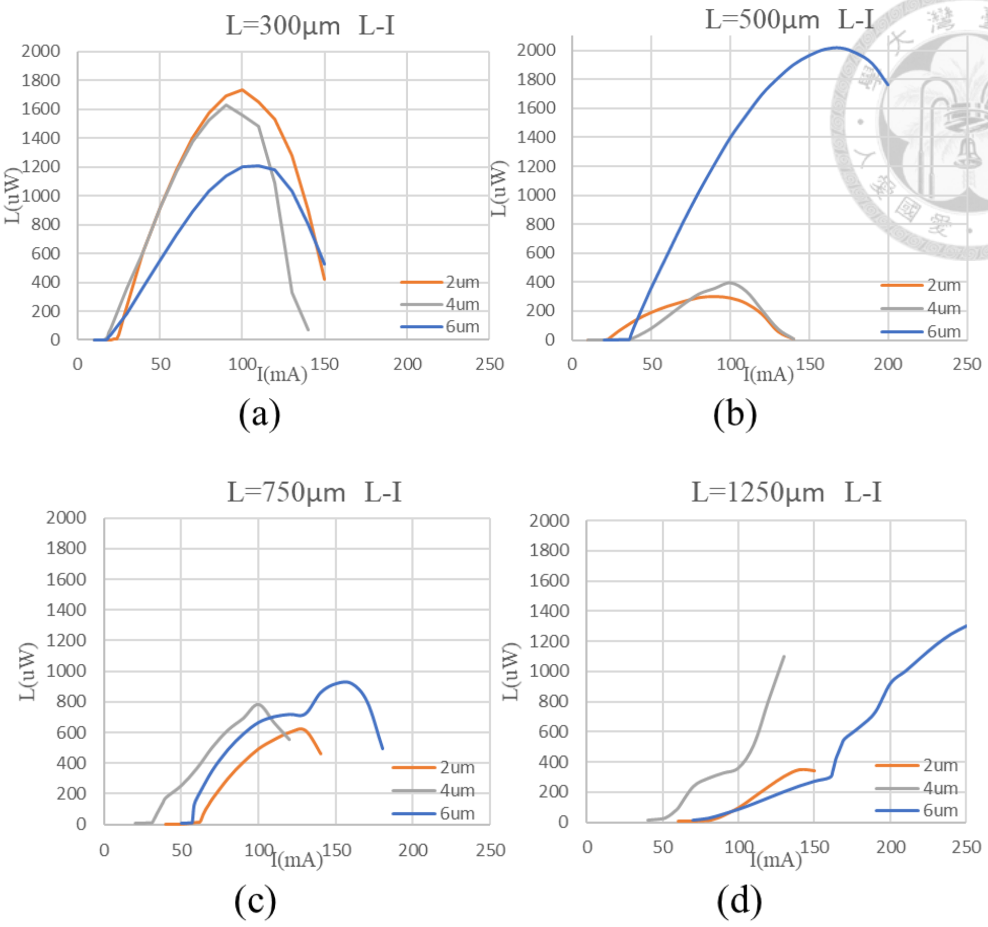

Figure 31 L-I characteristics comparison of R331 devices of various ridge width with (a) cavity length= 300μm; (b) cavity length= 500μm; (c) cavity length =750μm; (d) cavity length= 1250μm.

doi:10.6342/NTU202404706

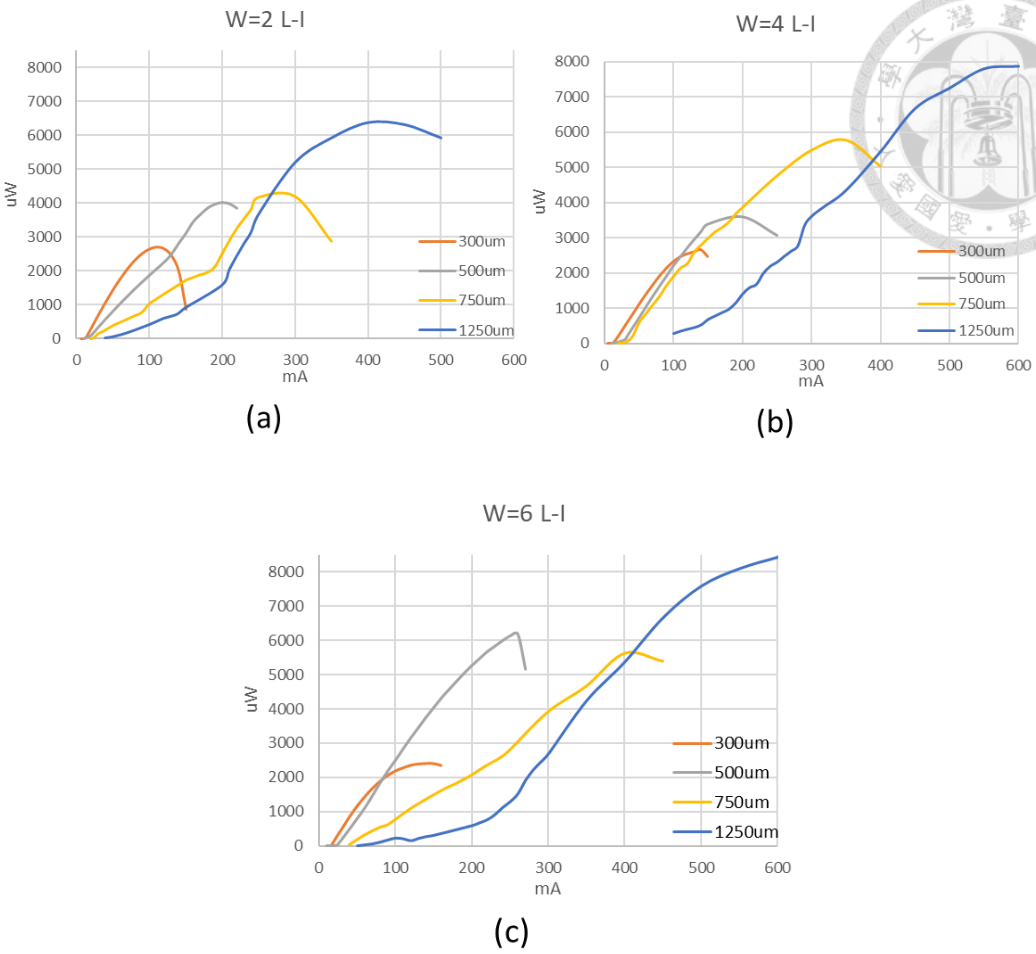

Figure 32 L-I characteristics comparison of UOC devices of various cavity lengths with (a) ridge width= 2μm; (b)ridge width= 4μm; (c)ridge width= 6μm.

doi:10.6342/NTU202404706

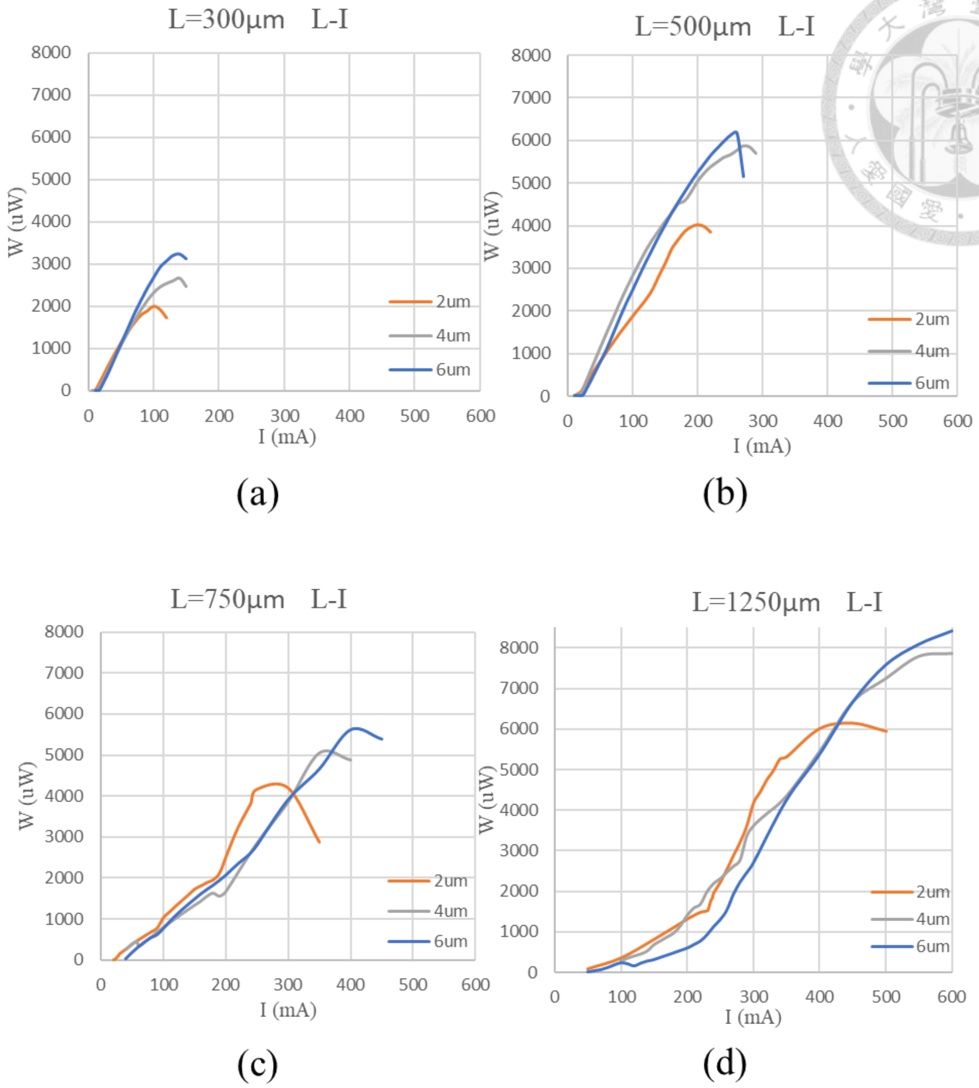

Figure 33 L-I characteristics comparison of UOC devices of various ridge width with (a) cavity length= 300μm; (b) cavity length= 500μm; (c) cavity length =750μm; (d) cavity length= 1250μm.

In **Figure 30** and **Figure 31**, the R331 devices showed us that the L-I curve of the long cavities (750, 1250μm) are prone to be twisted when applied larger current, while short ones (300, 500μm) are performing smoother. Also, the threshold current is higher

doi:10.6342/NTU202404706

as the cavity is longer. Furthermore, the performance of the L500/W6 um device reaches a maximum power of 2mW and maintained a non-twisted curve during operation.

As for the UOC devices showed in **Figure 32** and **Figure 33**, the maximum output power could reach larger in comparison to that of R331 ones generally. The highest output light power is performed by the L1250/W6 device, reaching about 8.4 (8.43) mW. Here we could easily see the point of input current resulting in roll-over is larger as cavity gets longer, and the threshold current Ith is higher as well. [Note that in **Figure 32** and **Figure 33**, for a more similar trend to that of other plots, some devices under same size (for instance, L300/W2) may not be the same. As long as the geometry of the component—such as ridge width and cavity length—is the same, we can consider them as the same type of component.]

4.2.2 Threshold Current of the DFB Lasers

From the L-I curves we mentioned previously, we could then acquire the threshold current Ith of each component. The comparison of different sizes is shown in **Figure 34**. For both version devices, the Ith is larger as the cavity length gets longer, meaning it requires higher input current to start lasing.

doi:10.6342/NTU202404706

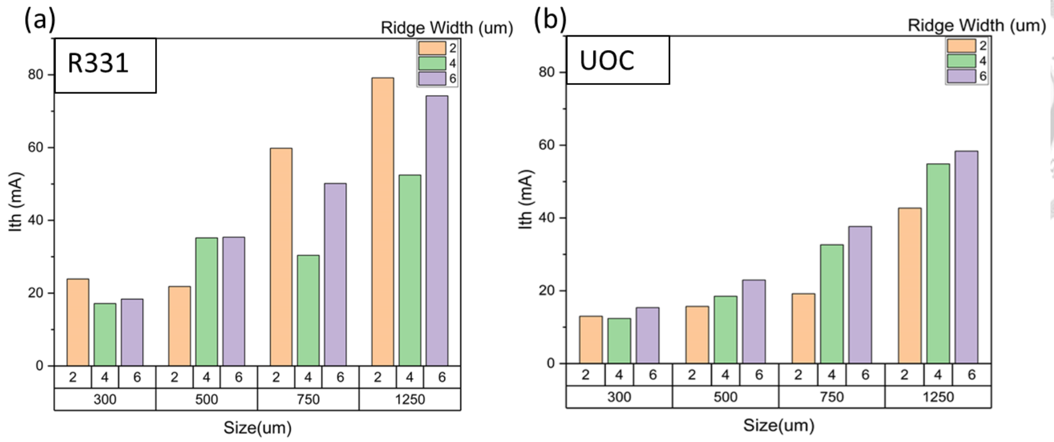

Figure 34 Threshold current Ith of each size of (a)R331 (b)UOC components.

4.2.3 Internal Loss α_i

Internal loss in a laser refers to the loss of optical power within the laser cavity, mainly caused by light scattering and material absorption. The losses reduce the laser's efficiency and output power. Thus, optimizing the cavity's materials and design is essential to minimize losses and improve performance. To acquire α_i, we utilized **Equation 7** [35] below, then plot $\frac{1}{\eta_d}$ as Y-axis and L as X-axis. Finally, combining the intercept η_i and slope $\frac{2\alpha_i}{\eta_i \cdot ln\left(\frac{1}{R_1R_2}\right)}$, we're able to extract the internal loss α_i.

Figure 35 The internal loss α_i of (a) R331 (b) UOC devices under different width. The 2μm wide R331 device has an enormous loss, which might be caused by the fact the ridge width is too slim and could be easier to be harmed, also a poor mirror coating quality during the fabricating process, leading to a scattering of light and reduces the output light power.

doi:10.6342/NTU202404706

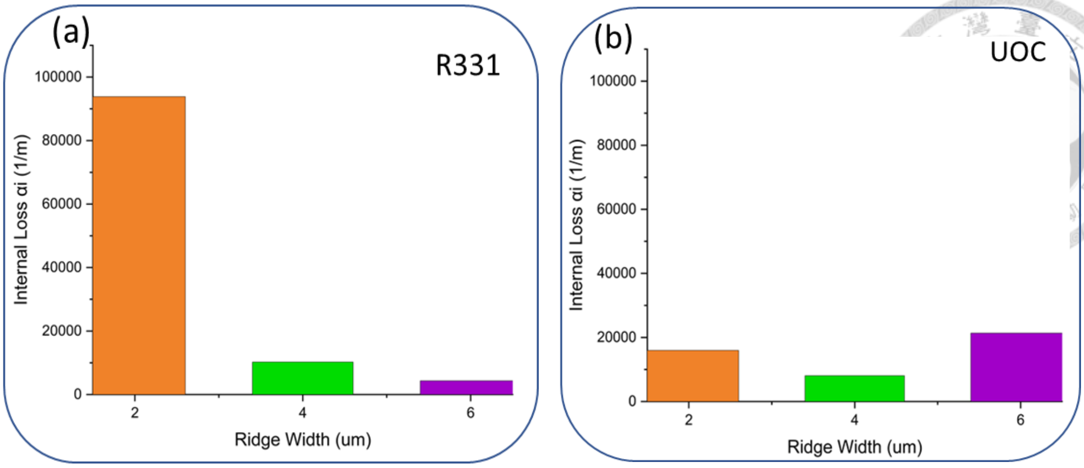

Figure 35 The internal loss α_i of (a) R331 (b) UOC devices under different width.

- $$\frac{1}{\eta_d} = \frac{1}{\eta_i}[1 + \frac{2\alpha_i}{ln(\frac{1}{R_1 R_2})} L]$$ **Equation 7** [35]

-ηd= $\frac{\Delta P/\Delta I}{hc/q\lambda}$ (External Differential Quantum Efficiency)

-L: Cavity length

-R_1, R_2: Reflectivity of front& rear mirrors (≒0.00025& 0.909, provided by UOC)

-η_i :Internal Quantum Efficiency, change in output light power over the change in input current ($\frac{\Delta P}{\Delta I}$)

doi:10.6342/NTU202404706

4.2.4 Spectrum of the DFB Lasers

Here, we focus on the spectra of certain components, which are sufficient to explain the spectral performance of the vast majority of components. In **Figure 36**, (a) L300/W2, (b) L500/W6, (d) L750/W6, and (e) L1250/W2 showed single-mode operation, yet in (a) and (d) the mode-hopping occurred under the input current of 70 and 60 mA, respectively. On the other hand, both (c) L750/W4 and (f) L1250/W6 showed the multimode phenomenon that happened to the majority of long-cavity devices (750& 1250μm) we fabricated.

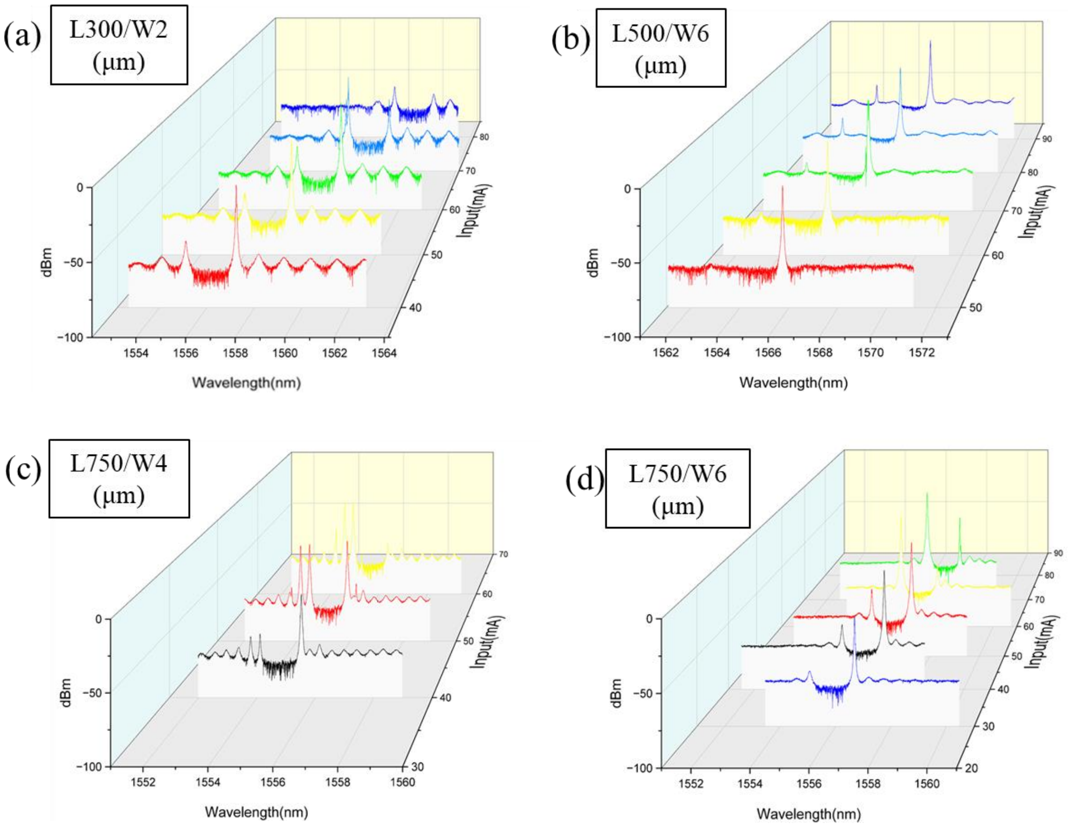

doi:10.6342/NTU202404706

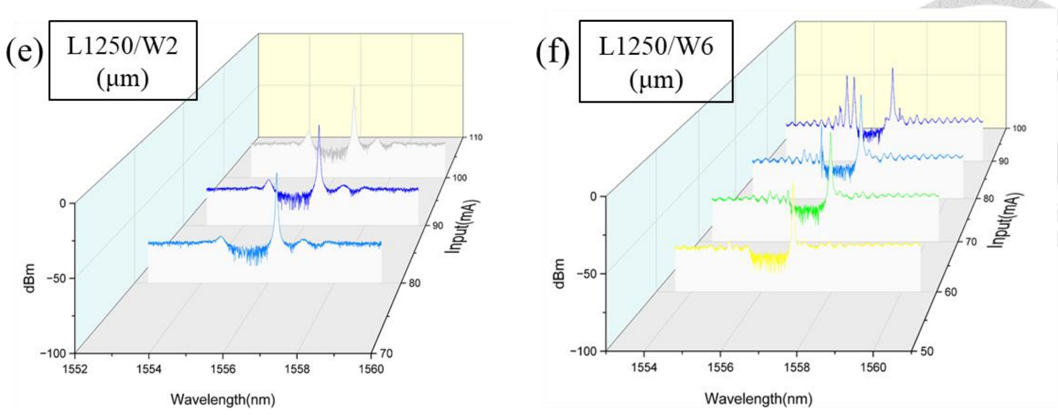

Figure 36 The spectrum diagram of the R331 components under various input current (a) L300/W2 (b) L500/W6 (c) L750/W4 (d) L750/W6 (e) L1250/W2 (f) L1250/W6 μm. To distinguish between different geometries of the lasers, L300 means 300-micron cavity, and W2 means 2-micron ridge width.

In **Figure 37**, four spectrum diagrams of (a) L300/W4 (b) L500/W4 (c) L750/W4 (d) L1250/W4 μm could represent most of the situations we observed. Aside from (a) L300/W4, the three others were operated in multimode. Unfortunately, the long-cavity (750& 1250μm) UOC devices could hardly work as single-mode.

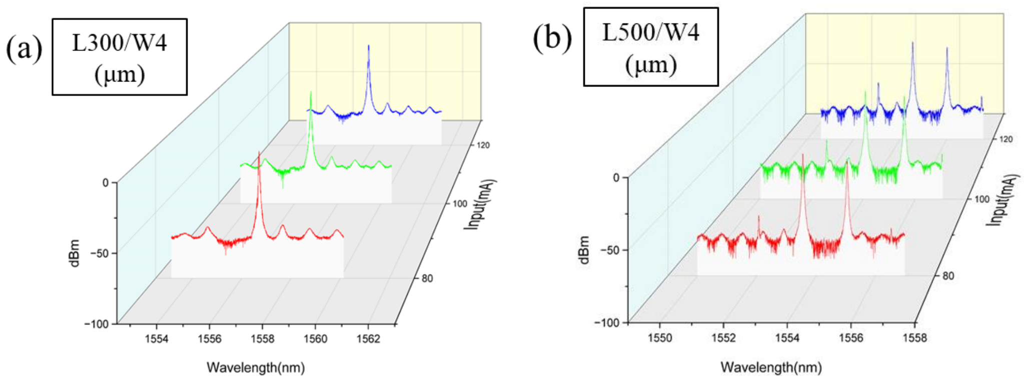

doi:10.6342/NTU202404706

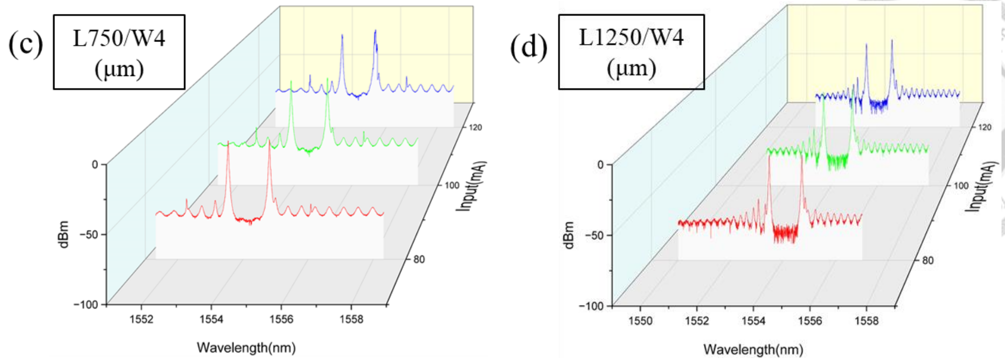

Figure 37 The spectrum diagram of the UOC components under various input current (a) L300/W4 (b) L500/W4 (c) L750/W4 (d) L1250/W4 μm. To distinguish between different geometries of the lasers, L750 means 750-micron cavity, and W4 means 4-micron ridge width.

Chapter5 Discussion and Conclusion

Firstly, regarding the L-I characteristics of the R331 and UOC components, the generally lower optical power of R331 compared to UOC can be attributed to several factors. Although the same process steps are followed, differences in cleanroom processing equipment may play a role. During dry etching, equipment instability can sometimes lead to over-etching, potentially harming the active layer where radiative recombination occurs. Furthermore in **Figure 38**, the passivation layer (Si_3N_4) on the **(a)** R331 components exhibits poor adhesion and a rough surface compared to **(b)** UOC ones, raising concerns about its ability to adequately protect the components.

doi:10.6342/NTU202404706

Additionally, the quality of gold plating during contact formation and subsequent chemical gold plating may also contribute to the difference.

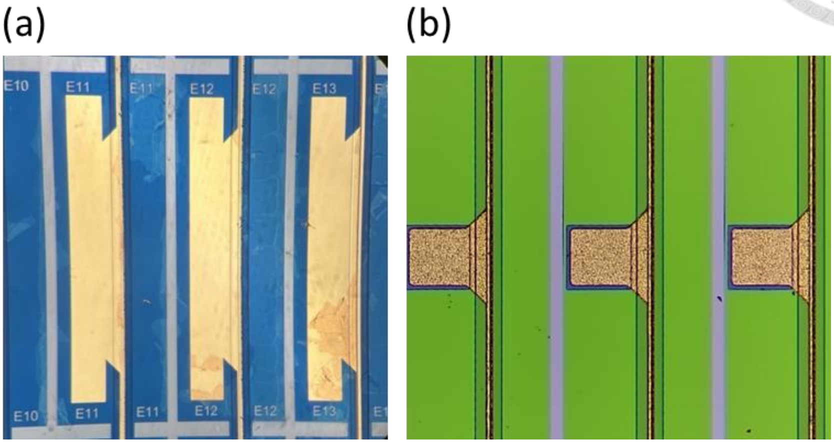

Figure 38 The photos taken from optical microscope of (a) R331 (b) UOC devices

5.1 Heat Influences

5.1.1 Heat Impedance Zth

Here we calculate the heat impedance Zth of both R331 and UOC long-cavity (750& 1250μm) devices via **Equation 8** [36, 37]. The equation on the left is essentially size-dependent and serves as the ideal reference value. The equation on the right is calculated using the actual measured power and temperature. This compares the theoretical and actual thermal impedance of the component.

doi:10.6342/NTU202404706

$$Zth = \frac{ln\,(4h/w)}{\pi kl} = \frac{\Delta T}{IV - Popt} \qquad \textbf{Equation 8}$$

h is the thickness of the ridge and substrate;

w and *l* represent as the ridge width and length;

k is the thermal conductivity of InP, refer to the chart in [38];

ΔT is the temperature between device and the ambient;

Popt is the measured output light power.

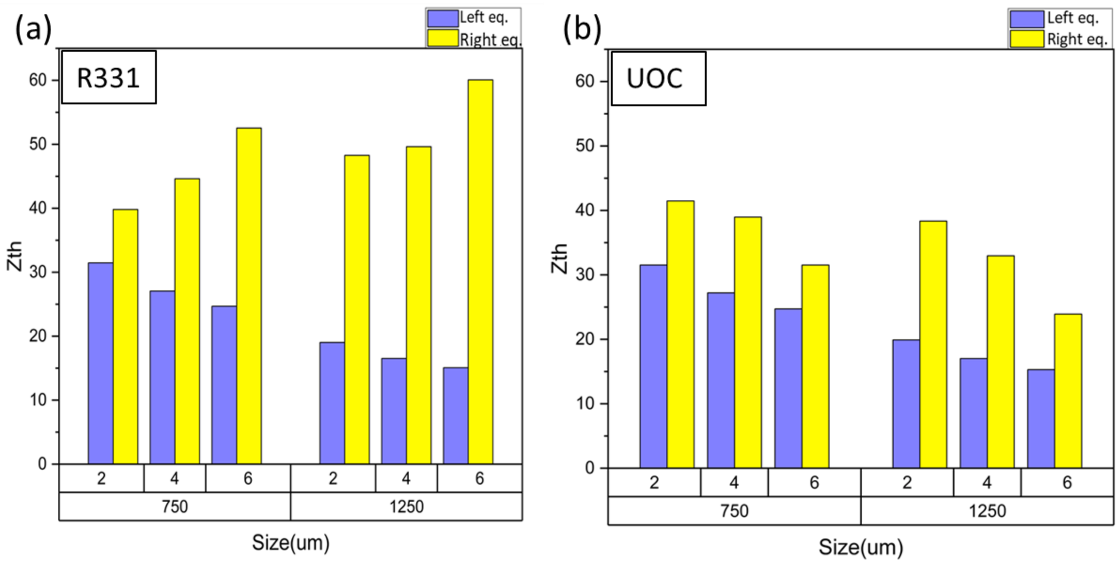

Figure 39 The heat impedance Zth calculated from **Equation 8**

Figure 39 shows the heat impedance Zth of both R331 and UOC devices, the left equation's results show that as the size gets smaller, the heat impedance should as well

doi:10.6342/NTU202404706

decrease. The UOC results from right equation do follow the trend while R331 ones don't. This can help explain why the R331 components generally have lower optical power compared to the UOC components, as well as why they experience the roll-over phenomenon earlier, which is due to thermal limitations. The presence of defects in larger components, uneven current distribution, and heat concentration at specific locations can contribute to inefficient heat dissipation, leading to a quicker thermal build-up. This thermal effect can cause the device to reach its thermal rollover point sooner, resulting in a drop in performance.

5.1.2 Temperature/Current Dependence on Wavelength

Later we calculated the temperature dependence on wavelength (Δλpeak/ ΔT) and current dependence on wavelength (Δλpeak/ ΔI) of the R331 device with L750/ W6 and L1250/W2 devices under single-mode operation. For the L750/W6 device, **Δλpeak/ΔT= 0.272 (nm/ °C)** and **Δλpeak/ ΔI= 0.0408 (nm/ mA)**, while **Δλpeak/ΔT= 0.525 (nm/ °C)** and **Δλpeak/ ΔI= 0.0105 (nm/ mA)** for the L1250/W2 one. As references, **Figure 40** showed the wavelength shift with temperature in the 3^{rd} benchmark [39] of (0.1 nm/ °C) is smaller than both of ours (0.272 & 0.525 nm/ °C). As for the current impedance on wavelength in 1^{st} [40]and 2^{nd} [41]benchmark, the L750/W6 device (0.0408 nm/ mA) is higher than both of them (0.015 – 0.031 nm/ mA)

doi:10.6342/NTU202404706

, while the L1250/W2 one is a bit lower (0.0105 nm/ mA). These summed up that the R331 fabricated lasers' wavelength shift due to the temperature and current increase is higher than expected.

Benchmark	Wavelength Range	QW Material	Δλ/ΔI or Δλ/ΔT	Paper Information
1	1550nm	not mentioned	0.024 – 0.031 nm/ mA	Renjia Guo,1 Jun Lu,1 Shengping Liu,1 Yuechun Shi,1 Yating Zhou,2 Yutao Chen,1 Jia Luan,1 and Xiangfei Chen,1 Senior Member, IEEE, "Multisection DFB Tunable Laser Based on REC Technique and Tuning by Injection Current", Vol. 8, No. 4, page #5 , August 2016
2	1550nm	InAlGaAs	0.015 nm/ mA	Hartmut Hillmer, S. Hansmann, Herbert Burkhard, Herbert Walter, Alois Krost, and Dieter Bimberg, Member, IEEE, "Study of Wavelength Shift in InGaAs/ InAlGaAs QW DFB Lasers Based on Laser Parameters From a Comparison of Experiment and Theory", IEEE JOURNAL OF QUANTUM ELECTRONICS, VOL. 30. NO. 10, page #5, OCTOBER 1994
3	1550nm	InGaAsP/InP	1Å/ K (0.1 nm/ °C)	Shigeyuki Akiba,"Temperature Dependence of Lasing Characteristics of InGaAsP/InP Distributed Feedback Lasers in 1.5 μm Range" et al 1982Jpn. J. Appl. Phys.21 1736, page #5 , 1982

Figure 40 The benchmark as the reference values of Δλpeak/ ΔT and Δλpeak/ ΔI

5.2 Mode-hopping and Multimode

Several factors may contribute to the unexpected multimode: the AR coating might have a higher reflectivity than expected, the grating or cleaved facet could be damaged as in (e.g., due to poor adhesion of the passivation layer); the initial gain might not be aligned and optimized for the correct wavelength, causing mode hopping as the current is increased; and there might be misalignment between the ridge and grating during

doi:10.6342/NTU202404706

process, this has a more severe impact on long cavity components because, under the same angular deviation, the ends (cleaved facet) of longer components deviate more compared to the shorter ones.

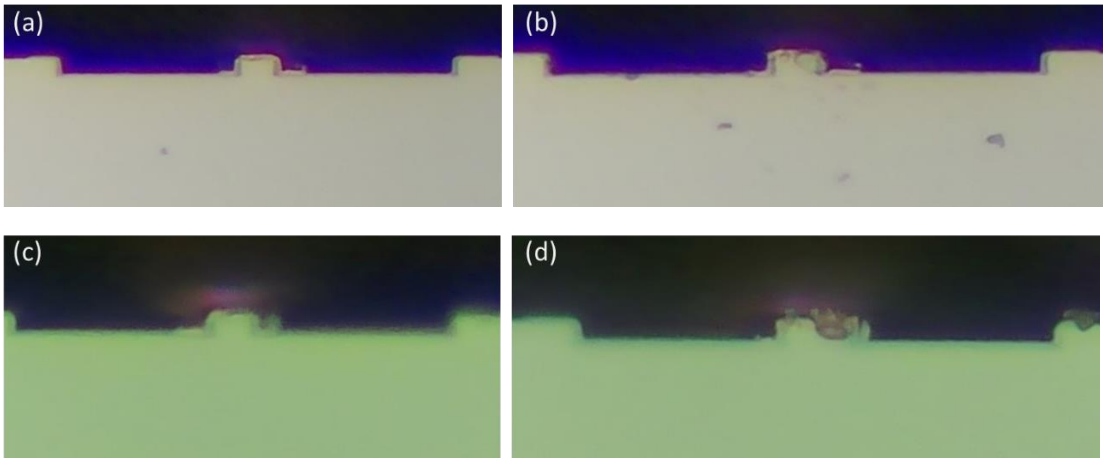

Figure 41 The photo taken from optical microscope of **(a)** Intact AR **(b)** Damaged AR **(c)** Intact HR **(d)** Damaged HR facets

For the potential coating issues, we calculated the F ratio, which is determined as ratio of light power emitted from front facet over total in **Equation 9**[36], to see if the actual value of reflectivity is varied from the parameter provided by UOC.

$$F = \frac{Pfront}{Ptotal} = \frac{1-R_f^2}{\left(1-R_f^2\right)+\frac{R_f}{R_b}\left(1-R_b^2\right)}$$ **Equation 9**[36]

- $R_{f,b}$ is the reflectivity of front/rear (AR/HR) facet.

doi:10.6342/NTU202404706

Thus, we took the reflectivity parameters provided by UOC (Rf= 0.03%; Rb= 90%) into the right equation as the ideal F (= 99.9% in any size), while the power we measured into the left side. In **Figure 42**, the F ratio values ranged from 0.75 to 0.96, which is discrepancy between the expected and actual reflectivity. It might cause to the misalign of gain spectrum, especially from the AR side, due to the inability to precisely control the phase at the cleavage point, an AR coating is needed to be applied to ignore the uncertain grating phase at the cleavage area.

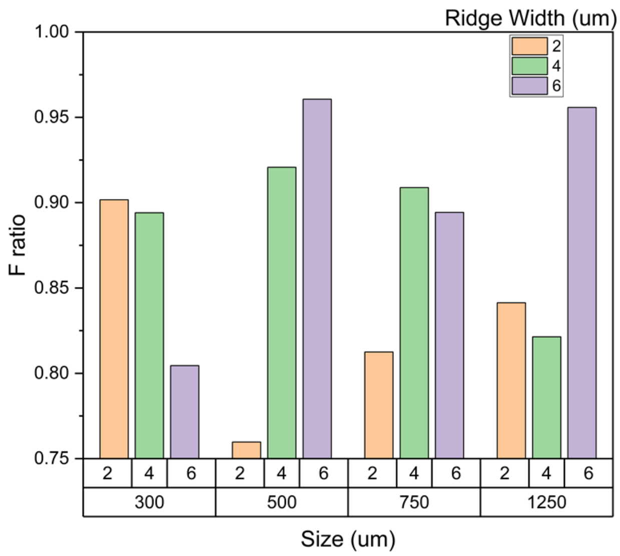

Figure 42 F ratio calculated from the power we measured. [Note that here we only conduct the verification on the UOC devices since R331 ones are quite unstable even driving with same currents.]

doi:10.6342/NTU202404706

5.3 Conclusion and Future Work

This article primarily explores the feasibility of fabricating long resonator ridge waveguide DFB lasers using the processing capabilities available in the on-campus cleanroom. It also investigates potential errors that may arise during the process by examining the performance of the finished components, including power, spectral modes, thermal influences, and other factors.

Some areas for future improvement include: when etching the ridge structure, it is essential to ensure that the grating and ridge directions are aligned and to verify the etching depth each time to prevent over-etching, which could damage the active layer and grating, resulting in suboptimal power and spectral performance. Additionally, the quality of the passivation layer must be ensured during coating to prevent oxidation of the component's surface. Finally, attention should be paid to the cleaving process to avoid rough or uneven surfaces that could affect the quality of subsequent coating.

doi:10.6342/NTU202404706

Appendices

A. Ith

R331:

Ith				
校內	300	500	750	1250
2	23.91	21.84	59.82	79.15
4	17.16	35.19	30.41	52.45
6	18.37	35.37	50.13	74.22

UOC:

Ith				
Circle	300	500	750	1250
2	9.5	14.6	21.7	36.1
4	12.3	25.9	30.4	52.8
6	15.8	21.7	38.7	58.0
Ith				
Square	300	500	750	1250
2	13.0	15.7	19.2	42.7
4	12.4	18.5	32.6	54.8
6	15.4	22.9	37.7	58.4

B. Ideality factor n

Size		R331	UOC
L(um)	W(um)	n	
300	2	2.5	2.6
	4	1.5	2.6
	6	1.6	4.2
500	2	1.6	2.3
	4	1.6	4.7
	6	1.5	2.4
750	2	1.6	2.5
	4	1.5	1.8
	6	1.5	2.1
1250	2	2.1	2.8
	4	3.5	2.5
	6	1.5	3.0

C. R331 Spectrum

doi:10.6342/NTU202404706

300 2 (Single mode+ Mode shift)

I= 40mA		I= 50mA		I= 60mA		I= 70mA		I= 80mA	
Stopband	2.114	Stopband	2.102	Stopband	2.164	Stopband	2.16	Stopband	2.228
SMSR	39.891	SMSR	39.774	SMSR	35.74	SMSR	17.953	SMSR	6.714
Peak	1557.234	Peak	1558.132	Peak	1559.162	Peak	1558.304	Peak	1566.814

500 6 (Single mode)

I= 50mA		I= 60mA		I= 70mA		I= 80mA		I= 90mA	
Stopband	2.948	Stopband	2.946	Stopband	1.962	Stopband	1.966	Stopband	1.9739
SMSR	55.257	SMSR	53.776	SMSR	51.954	SMSR	44.851	SMSR	42.305
Peak	1565.736	Peak	1566.078	Peak	1566.51	Peak	1566.814	Peak	1567.218

750 4 (Multi-mode)

I= 80mA		I= 90mA		I= 100mA	
Stopband	1.42	Stopband	1.418	Stopband	1.426
SMSR	30.478	SMSR	2.593	SMSR	0.764
Peak	1555.524	Peak	1555.892	Peak	1554.584

750 6 (Single mode+ Mode shift)

I= 30mA		I= 40mA		I= 50mA		I= 60mA		I= 70mA	
Stopband	1.612	Stopband	1.612	Stopband	1.598	Stopband	1.544	Stopband	1.458
SMSR	38.459	SMSR	41.265	SMSR	37.225	SMSR	40.206	SMSR	22.144
Peak	1556.682	Peak	1556.958	Peak	1557.256	Peak	1556.074	Peak	1556.484

1250 2 (Single mode)

I= 80mA		I= 90mA		I= 100mA	
Stopband	1.678	Stopband	1.66	Stopband	1.62
SMSR	46.327	SMSR	44.51	SMSR	39.023
Peak	1556.264	Peak	1556.478	Peak	1556.688

1250 6 (Multi-mode)

I= 60mA		I= 70mA		I= 80mA		I= 90mA	
Stopband	1.316	Stopband	1.31	Stopband	1.31	Stopband	1.368
SMSR	41.049	SMSR	43.862	SMSR	25.167	SMSR	6.752
Peak	1556.912	Peak	1557.068	Peak	1557.172	Peak	1557.458

D. UOC Spectrum

300 4 square (Single mode)

I= 100mA		I= 110mA		I= 120mA	
Stopband	2.172	Stopband	2.204	Stopband	2.216
SMSR	55.247	SMSR	55.198	SMSR	55.931
Peak	1557.122	Peak	1558.3	Peak	1559.59

500 4 square (Multi-mode)

I= 80mA		I= 100mA		I= 120mA	
Stopband	1.502	Stopband	1.492	Stopband	1.48
SMSR	4.894	SMSR	4.12	SMSR	5.007
Peak	1553.548	Peak	1554.088	Peak	1554.546

750 4 square (Multi-mode)

I= 80mA		I= 100mA		I= 120mA	
Stopband	1.2701	Stopband	1.27	Stopband	1.312
SMSR	0.775	SMSR	2.27	SMSR	4.499
Peak	1544.812	Peak	1555.144	Peak	1555.586

1250 4 square (Multi-mode)

I= 80mA		I= 100mA		I= 120mA	
Stopband	1.238	Stopband	1.24	Stopband	1.24
SMSR	0.362	SMSR	2.883	SMSR	4.87
Peak	1554.716	Peak	1554.912	Peak	1555.12

E. Heat Impedance Zth

doi:10.6342/NTU202404706

R331

$$Zth = \frac{ln(4h/w)}{\pi kl} \text{ (Left)}$$

750					1250				
I	W	T	K	Zth	I	W	T	K	Zth
60	2	23.5	75.2	30.93	60	2	25	74.74	18.67
80	2	26.7	74.1	31.39	80	2	28.7	73.44	19.00
100	2	30	72.47	32.10	100	2	33	71.91	19.41
60	4	21.1	76.13	26.69	60	4	24	75.1	16.23
80	4	24	75.11	27.05	80	4	27.5	73.8	16.52
100	4	27	74	27.46	100	4	31.5	72.4	16.84
60	6	20.5	76.4	24.34	60	6	23	75.5	14.78
80	6	23.5	75.2	24.73	80	6	27	74	15.08
100	6	26	74.4	25.00	100	6	31	72.6	15.37

$$Zth = \frac{\Delta T}{IV - Popt} \text{ (Right)}$$

750						1250					
I	W	L	ΔT	V	Zth	I	W	L	ΔT	V	Zth
60	2	16	6.5	2.7	39.99	60	2	5	8	2.6	50.62
80	2	301	9.7	3.0	40.04	80	2	10	11.7	3.1	47.69
100	2	497	13	3.3	39.44	100	2	95	16	3.4	46.50
60	4	366	4.1	1.8	38.45	60	4	91.2	7	2.4	48.64
80	4	616	7	1.9	46.17	80	4	290	10.5	2.6	49.87
100	4	786	10	2.0	49.21	100	4	360	14.5	2.9	50.39
60	6	179	3.5	1.3	43.56	60	6	17.16	6	1.8	54.44
80	6	317	6.5	1.4	56.23	80	6	99	10	2.0	62.13
100	6	316	9	1.6	57.81	100	6	179.5	14	2.2	63.66

UOC

$$Zth = \frac{ln(4h/w)}{\pi kl} \text{(Left)}$$

750					1250				
I	W	T	K	Zth	I	W	T	K	Zth
100	2	22	75.8	30.69	150	2	29.6	73	19.12
150	2	28	73.63	31.59	300	2	37.7	70.34	19.84
200	2	33	72	32.31	400	2	47.5	67.2	20.77
100	4	22	75.8	26.81	150	4	25.5	74.5	16.36
150	4	24.2	75.1	27.06	300	4	33.9	71.6	17.03
200	4	29.3	73.2	27.76	400	4	42.1	68.9	17.69
100	6	20.1	76.5	24.31	150	6	22.7	75.5	14.78
150	6	23.5	75.2	24.73	300	6	30.3	72.7	15.35
200	6	26.8	74	25.13	400	6	36	70.9	15.74

$$Zth = \frac{\Delta T}{IV - Popt} \text{(Right)}$$

750						1250					
I	W	L	ΔT	V	Zth	I	W	L	ΔT	V	Zth
100	2	1321	5	1.36	37.12	150	2	1154.5	12.6	1.52	55.54
150	2	2125	11	1.63	45.38	300	2	5592	20.7	2.24	31.13
200	2	2909	16	1.92	41.92	400	2	6380	30.5	2.71	28.34
100	4	866	5	1.20	41.97	150	4	868	8.5	1.38	41.23
150	4	1465	7.2	1.38	35.03	300	4	4064	16.9	1.91	29.72
200	4	1900	12.3	1.55	39.92	400	4	5450	25.1	2.26	27.90
100	6	856	3.1	1.14	27.40	150	6	384	5.7	1.43	26.62
150	6	1673	6.5	1.31	33.36	300	6	2862	13.3	1.90	23.51
200	6	2322	9.8	1.46	33.83	400	6	5380	19	2.21	21.60

doi:10.6342/NTU202404706

Reference

1. Etrillard, J., et al., *New self-aligned processes for III–V electronic high speed devices.* Journal of Vacuum Science & Technology B: Microelectronics and Nanometer Structures Processing, Measurement, and Phenomena, 1999. **17**(4): p. 1510-1515.
2. Einstein, A., *7. Zur Quantentheorie der Strahlung*, in *Quantentheorie*. 1969, De Gruyter: Berlin, Boston. p. 209-228.
3. Schawlow, A.L. and C.H. Townes, *Infrared and Optical Masers.* Physical Review, 1958. **112**(6): p. 1940-1949.
4. Kogelnik, H. and C.V. Shank, *Stimulated Emission in a Periodic Structure.* Applied Physics Letters, 1971. **18**(4): p. 152-154.
5. Suematsu, Y., *Long-wavelength optical fiber communication.* Proceedings of the IEEE, 1983. **71**(6): p. 692-721.
6. Arnon, S. and N.S. Kopeika, *Laser satellite communication network-vibration effect and possible solutions.* Proceedings of the IEEE, 1997. **85**(10): p. 1646-1661.
7. Collis, R.T.H., *Lidar.* Applied Optics, 1970. **9**(8): p. 1782-1788.
8. Peng, Q., et al., *Lasers in medicine.* Reports on Progress in Physics, 2008. **71**(5): p. 056701.
9. Kaushal, H. and G. Kaddoum, *Applications of Lasers for Tactical Military Operations.* IEEE Access, 2017. **5**: p. 20736-20753.
10. *The Laser Turns 60! - SPIE*. Available from: https://spie.org/news/spie-celebrates-the-60th-anniversary-of-the-laser#_=_.
11. Koyama, F., *Recent Advances of VCSEL Photonics.* Journal of Lightwave Technology, 2006. **24**(12): p. 4502-4513.
12. Sorokin, P.P., J.D. Axe, and J.R. Lankard, *Spectral Characteristics of GaAs Lasers Operating in ``Fabry-Perot'' Modes.* Journal of Applied Physics, 1963. **34**(9): p. 2553-2556.
13. Tadokoro, T., et al., *43 Gb/s 1.3 μm DFB Laser for 40 km Transmission.* Journal of Lightwave Technology, 2012. **30**(15): p. 2520-2524.
14. Grimaldi, M.G., P. Baeri, and E. Rimini, *Laser-induced free-carrier absorption in Si single crystal.* Applied Physics A, 1984. **33**(2): p. 107-111.
15. Siegman, A.E., *Unstable optical resonators for laser applications.* Proceedings of the IEEE, 1965. **53**(3): p. 277-287.

doi:10.6342/NTU202404706

16. Kogelnik, H. and C.V. Shank, *Coupled-Wave Theory of Distributed Feedback Lasers.* Journal of Applied Physics, 1972. **43**(5): p. 2327-2335.
17. Weber, J.P. and S. Wang, *A new method for the calculation of the emission spectrum of DFB and DBR lasers.* IEEE Journal of Quantum Electronics, 1991. **27**(10): p. 2256-2266.
18. Grillot, F., *On the Effects of an Antireflection Coating Impairment on the Sensitivity to Optical Feedback of AR/HR Semiconductor DFB Lasers.* IEEE Journal of Quantum Electronics, 2009. **45**(6): p. 720-729.
19. Soref, R., *The Past, Present, and Future of Silicon Photonics.* IEEE Journal of Selected Topics in Quantum Electronics, 2006. **12**(6): p. 1678-1687.
20. Johnson, J.E., et al. *Performance and Reliability of Advanced CW Lasers for Silicon Photonics Applications*. in *2022 Optical Fiber Communications Conference and Exhibition (OFC)*. 2022.
21. Wang, H., et al. *High-Power Wide-Bandwidth 1.55-μm Directly Modulated DFB Lasers for Free Space Optical Communications*. in *Conference on Lasers and Electro-Optics*. 2019. San Jose, California: Optica Publishing Group.
22. Bagaeva, O.O., et al., *Experimental studies of 1.5 – 1.6 μm high-power single-frequency semiconductor lasers.* Quantum Electronics, 2020. **50**(2): p. 143.
23. Mao, Y., et al. *Record-High Power 1.55-μm Distributed Feedback Laser Diodes for Optical Communication*. in *2021 Optical Fiber Communications Conference and Exhibition (OFC)*. 2021.
24. Mao, Y., et al. *High Power Uncooled CW-DFB lasers with High Reliability*. in *2023 Optical Fiber Communications Conference and Exhibition (OFC)*. 2023.
25. Mikami, O., *1.55 μm GaInAsP/InP Distributed Feedback Lasers.* Japanese Journal of Applied Physics, 1981. **20**(7): p. L488.
26. Ishutkin, S., et al., *The Method of Low-Temperature ICP Etching of InP/InGaAsP Heterostructures in Cl2-Based Plasma for Integrated Optics Applications.* Micromachines, 2021. **12**(12): p. 1535.
27. Bortolotti, A., et al., *Optical Lithography*, in *Silicon Sensors and Actuators: The Feynman Roadmap*, B. Vigna, et al., Editors. 2022, Springer International Publishing: Cham. p. 169-201.
28. Lucovsky, G., et al., *Formation of thin film dielectrics by remote plasma-enhanced chemical-vapor deposition (remote PECVD).* Applied Surface Science, 1989. **39**(1): p. 33-56.

doi:10.6342/NTU202404706

29. Chen, B., F. Tay, and C. Iliescu, *Development of thick film PECVD Amorphous silicon with low stress for MEMS applications.* Proceedings of SPIE - The International Society for Optical Engineering, 2008. **7269**.
30. Layadi, N., J.I. Colonell, and J.T. Lee, *An introduction to plasma etching for VLSI circuit technology.* Bell Labs Technical Journal, 1999. **4**(3): p. 155-171.
31. Yang, S.K., et al., *New self-align method for fabrication of 980 nm ridge waveguide laser diodes.* Optical and Quantum Electronics, 1995. **27**(5): p. 447-451.
32. *Electron Beam Source for Electron Beam Deposition - JEOL*. Available from: https://www.jeol.com/products/science/eb.php.
33. Long, M. and J. Newman, *Image Reversal Techniques With Standard Positive Photoresist*. 1984 Microlithography Conferences. Vol. 0469. 1984: SPIE.
34. *LED 原理與應用*

Principles and Applications of Light-emitting Diode. Available from: https://www.wunan.com.tw/bookdetail?NO=10915.

35. 盧廷昌、王興宗, *半導體雷射導論*

Introduction to Semiconductor Lasers.

36. Larry A. Coldren, S.W.C., Milan L. Mashanovitch. *Diode Lasers and Photonic Integrated Circuits*. Available from: https://books.google.com.tw/books?id=D6Ub126rtPoC&printsec=frontcover&redir_esc=y#v=onepage&q&f=false.
37. Mickus, D., et al., *Method to measure thermal impedance for all-active lasers using the athermalisation condition.* Optics Continuum, 2022. **1**(3): p. 556-564.
38. Chaparala, S.C., et al., *Design Guidelines for Efficient Thermal Management of Mid-Infrared Quantum Cascade Lasers.* IEEE Transactions on Components, Packaging and Manufacturing Technology, 2011. **1**(12): p. 1975-1982.
39. Akiba, S., et al., *Temperature Dependence of Lasing Characteristics of InGaAsP/InP Distributed Feedback Lasers in 1.5 µm Range.* Japanese Journal of Applied Physics, 1982. **21**(12R): p. 1736.
40. Guo, R., et al., *Multisection DFB Tunable Laser Based on REC Technique and Tuning by Injection Current.* IEEE Photonics Journal, 2016. **8**(4): p. 1-7.
41. Hillmer, H., et al., *Study of wavelength shift in InGaAs/InAlGaAs QW DFB lasers based on laser parameters from a comparison of experiment and theory.* IEEE Journal of Quantum Electronics, 1994. **30**(10): p. 2251-2261.

doi:10.6342/NTU202404706